Inorganic Chemistry

Article

pubs.acs.org/IC

An Approach to More Accurate Model Systems for Purple Acid Phosphatases (PAPs)

Paul V. Bernhardt,[†] Simone Bosch,[†,‡] Peter Comba,[*,‡] Lawrence R. Gahan,[†] Graeme R. Hanson,[§,◆] Valeriu Mereacre,[⊥] Christopher J. Noble,[§] Annie K. Powell,[⊥,▽] Gerhard Schenk,[†] and Hubert Wadepohl[‡]

[†]School of Chemistry and Molecular Biosciences, The University of Queensland, Brisbane, QLD 4072, Australia

[‡]Anorganisch-Chemisches Institut and Interdisciplinary Center for Scientific Computing (IWR), Universität Heidelberg, Im Neuenheimer Feld 270, D-69120 Heidelberg, Germany

[§]Centre for Advanced Imaging, The University of Queensland, Brisbane, QLD 4072, Australia

[⊥]Institut für Anorganisch Chemie, Karlsruhe Institute of Technology (KIT), Engesserstr. 15, D-76131 Karlsruhe, Germany

[▽]Institute of Nanotechnology (INT), Karlsruhe Institute of Technology (KIT), P.O. Box 3640, D-76021 Karlsruhe, Germany

Supporting Information

ABSTRACT: The active site of mammalian purple acid phosphatases (PAPs) have a dinuclear iron site in two accessible oxidation states (Fe^{III}_2 and $Fe^{III}Fe^{II}$), and the heterovalent is the active form, involved in the regulation of phosphate and phosphorylated metabolite levels in a wide range of organisms. Therefore, two sites with different coordination geometries to stabilize the heterovalent active form and, in addition, with hydrogen bond donors to enable the fixation of the substrate and release of the product, are believed to be required for catalytically competent model systems. Two ligands and their dinuclear iron complexes have been studied in detail. The solid-state structures and properties, studied by X-ray crystallography, magnetism, and Mössbauer spectroscopy, and the solution structural and electronic properties, investigated by mass spectrometry, electronic, nuclear magnetic resonance (NMR), electron paramagnetic resonance (EPR), and Mössbauer spectroscopies and electrochemistry, are discussed in detail in order to understand the structures and relative stabilities in solution. In particular, with one of the ligands, a heterovalent $Fe^{III}Fe^{II}$ species has been produced by chemical oxidation of the Fe^{II}_2 precursor. The phosphatase reactivities of the complexes, in particular, also of the heterovalent complex, are reported. These studies include pH-dependent as well as substrate concentration dependent studies, leading to pH profiles, catalytic efficiencies and turnover numbers, and indicate that the heterovalent diiron complex discussed here is an accurate PAP model system.

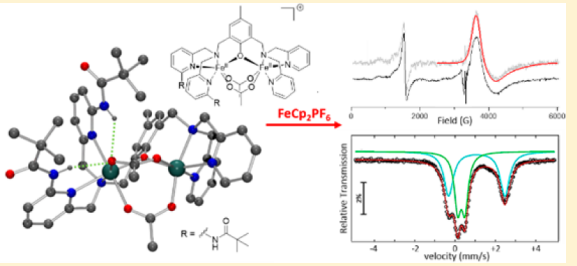

INTRODUCTION

Most nonheme iron proteins are involved in oxidation and oxygenation reactions by the interaction of their iron(II) form with dioxygen.[1−3] The subgroup of iron purple acid phosphatases (PAPs) perform hydrolysis via their heterovalent $Fe^{III}Fe^{II}$ or $Fe^{III}M^{II}$ (M = Zn, Mn) active site and is involved in the regulation of phosphate and phosphorylated metabolite levels in a wide range of organisms.[4,5] More precisely, PAPs catalyze the hydrolysis of phosphomonoesters at acidic to neutral pH. The active sites of the mammalian PAPs, isolated from bovine spleen (bsPAP) and porcine uterus (ufPAP), were shown to contain a dinuclear Fe center in two accessible oxidation states: the Fe^{III}_2 form, characterized by typical visible absorption maxima between 550 and 570 nm ($\varepsilon \approx 4000$ M^{-1} cm^{-1}), and the reduced $Fe^{III}Fe^{II}$ form, which exhibits blue-shifted absorption maxima between 505 and 510 nm ($\varepsilon \approx 4000$ M^{-1} cm^{-1}).[6−10] Interestingly, the Fe^{III}_2 form of ufPAP was found to have an upper limit of <1% of the activity of the heterovalent $Fe^{III}Fe^{II}$ form[11] and, therefore, PAPs are the only dinuclear metallohydrolases where the necessity for a heterovalent active site for catalysis has been established.[4,12] The redox potential of the $Fe^{III}_2/Fe^{III}Fe^{II}$ couple of ufPAP was found to be 0.367 V at pH 5 and 0.306 V at pH 6 vs NHE.[13] Because of this relatively low redox potential, the enzyme is easily and reversibly oxidized to the Fe^{III}_2 form.[14] This observation led to the suggestion that PAPs may regulate their catalytic activity *in vivo* by reversible oxidation/reduction of the active site.[13]

PAPs further differ from other nonheme diiron proteins by a tyrosinate ligand, which is responsible for the characteristic purple color. The corresponding absorption bands are assigned to tyrosinate-to-Fe^{III} charge transfer transitions.[8] With Mössbauer spectroscopy, the Fe centers of ufPAP and bsPAP were revealed to have different coordination spheres, and this was confirmed by single-crystal X-ray studies of ufPAP.[8,15,16] The magnetic susceptibility indicates that the Fe^{III} and Fe^{II} centers are weakly antiferromagnetically coupled with J values

Received: March 21, 2015

DOI: 10.1021/acs.inorgchem.5b00628
Inorg. Chem. XXXX, XXX, XXX−XXX

Chart 1. Previously Reported Diiron(III) Complexes with Second Sphere Hydrogen Bond Donors[21,22]

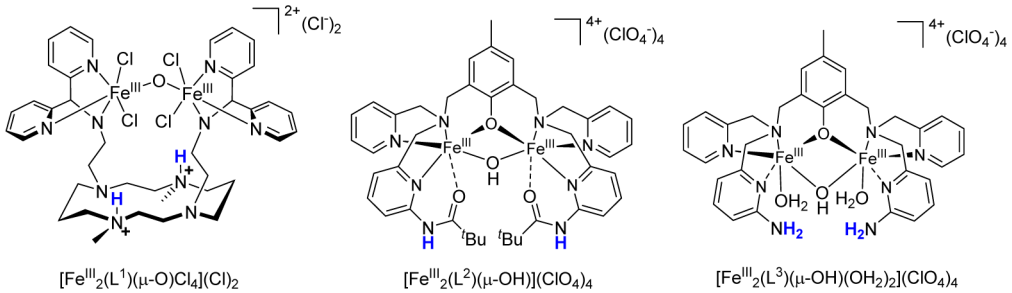

ranging from −5 cm^{-1} to −11 cm^{-1} ($H = -2JS_1S_2$),[8,17] and strong antiferromagnetic interactions were estimated in the oxidized Fe^{III}_2 form of ufPAP ($J > -150$ cm^{-1}).[8] The reduced heterovalent form of ufPAP exhibits rhombic EPR signals at g = 1.94, 1.73, and 1.58, consistent with an $S_T = 1/2$ ground state of an antiferromagnetically coupled *hs*Fe^{III}−*hs*Fe^{II} center.[6,18]

The activity of PAP enzymes is directly linked to bone resorption.[19] Therefore, detailed understanding of the catalytic mechanism of PAP may support the rational design of antiosteoporotic drugs.[20] In order to study the phosphoester hydrolysis mechanism of the active site of PAP, a variety of synthetic low-molecular-weight models have been developed. Structural, spectroscopic, and kinetic data of these have led to a substantial understanding of the catalytic reaction mechanism. The model substrates bis(dinitrophenyl)phosphate (BDNPP, phosphodiester) and dinitrophenylphosphate (DNPP, phosphomonoester) have frequently been used to investigate the activity of the model complexes. Although phosphodiester hydrolysis was observed with a wide range of model complexes, the biologically relevant hydrolysis of phosphomonoesters with model systems has rarely been reported. Recently, two dinuclear PAP models were developed, for which the hydrolysis of the phosphomonoester model substrate DNPP was achieved.[21,22] The two complexes, $[Fe^{III}_2(L^1)(\mu\text{-}O)Cl_4](Cl)_2$ and $[Fe^{III}_2(L^3)(\mu\text{-}OH)(OH_2)_2](ClO_4)_4$ (Chart 1), differ from previously studied model systems in their ability to form hydrogen bonds to the putative substrate molecule bound to the metal centers; this was accomplished by incorporation of basic residues adjacent to the dimetal core.

In recent years, many structural models for the active site of PAPs with phenoxido-containing multidentate ligands have been developed.[23] Fe^{III}_2 complexes of symmetric ligands were used to model the oxidized form of PAPs,[24−27] and heterovalent diiron complexes using asymmetric ligands were also generated and studied as structural PAP models.[13,28−31] From the separation of their one-electron redox processes, assigned to the $Fe^{II}_2/Fe^{III}Fe^{II}$ and $Fe^{III}Fe^{II}/Fe^{III}_2$ couples, the stability of the $Fe^{III}Fe^{II}$ form over the corresponding reduced and oxidized homovalent complexes was investigated. The comproportionation constant (K_{com}) for this equilibrium was found to be in the order of 10^{10}−10^{12} and, therefore, confirms the substantial stability of the mixed-valent $Fe^{III}Fe^{II}$ form.[23] One of the most widely employed $Fe^{III}Fe^{II}$ model complexes for the mixed-valent diiron active site of PAP is $[Fe^{III}Fe^{II}(BPBPMP)(\mu\text{-}OAc)_2]ClO_4$ (HBPBPMP = 2-{[bis-(pyridin-2-ylmethyl)amino]methyl}-6-{[2-hydroxybenzyl)-(pyridin-2-ylmethyl)amino]methyl}4-methylphenol; see Chart 2 for the ligand structure and models of similar complexes).[32−36] The bis-acetato-bridged $Fe^{III}Fe^{II}$ geometry with asymmetric ligands reveals significant similarities in the physical

Chart 2. Ligand Structures and Diiron(II) Complexes Discussed

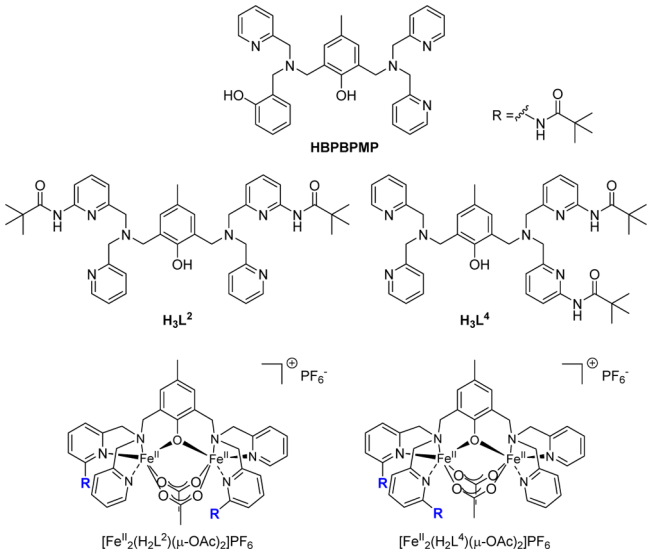

properties to the native ufPAP. In particular, $[Fe^{III}Fe^{II}(BPBPMP)(\mu\text{-}OAc)_2]ClO_4$ exhibits (i) a comparable metal−metal distance (3.483(2) Å vs 3.31 Å in ufPAP), (ii) a phenolate-to-Fe^{III} charge transfer at 550 nm (vs the tyrosinate-to-Fe^{III} charge transfer at ∼510 nm in ufPAP), (iii) weakly antiferromagnetically coupled *high-spin* Fe^{III} and Fe^{II} ions (J = −7.4 cm^{-1} vs −5 to −11 cm^{-1} in reduced ufPAP), (iv) localized iron valences in the solid state, and (v) a reversible $Fe^{III}Fe^{II}/Fe^{III}_2$ redox couple at a similar potential (380 mV vs NHE vs 344 mV at pH 4.1 and 367 mV at pH 5 for ufPAP).[32−36]

However, although $[Fe^{III}Fe^{II}(BPBPMP)(\mu\text{-}OAc)_2]ClO_4$ mimics accurately the first coordination sphere in the active site of PAP, the catalytic efficiency, with respect to phosphodiester hydrolysis, is modest and no monoesterase activity was reported. The PAP active site includes non-coordinated histidine groups proximal to the Fe centers that may help to position the substrate.[37] These second sphere interactions have been considered in diiron(III) complexes with basic groups proximal to the metal centers, in order to mimic the hydrogen bonding network within the active site of PAP (see Chart 1).[21,22] $[Fe^{III}_2(L^1)(\mu\text{-}O)(Cl_4)](Cl)_2$ was the first complex known to be able to hydrolyze phosphomonoesters.[22] The generation of the $Fe^{III}Fe^{II}$ form of $[Fe^{III}_2(L^3)(\mu\text{-}OH)\text{-}(OH_2)_2]^{2+}$ was achieved by bulk electrolysis,[21,38] and for HL^3 the $Fe^{III}Fe^{II}$ complex revealed a 5-fold increased catalytic efficiency with respect to the Fe^{III}_2 analogue, and this was proposed to be due to a significantly lower substrate affinity of the Fe^{II} center.[21]

DOI: 10.1021/acs.inorgchem.5b00628
Inorg. Chem. XXXX, XXX, XXX−XXX

The paradigm for the construction of more efficient structural and functional PAP mimetics is asymmetry (discrimination between trivalent and divalent iron as well as stabilization of a heterodinuclear active site), and the ability for hydrogen bonding to the substrate and/or nucleophile. The pivaloylamide-substituted ligand H_3L^4 (see Chart 2) provides two different coordination pockets, where the H-donor-substituted site is sterically more demanding. The two isomers with two amide residues adjacent to one Fe(II) center in the case of $[Fe^{II}_2(H_2L^4)(\mu\text{-}OAc)_2]PF_6$ or one amide residue adjacent to each Fe(II) center in the case of $[Fe^{II}_2(H_2L^2)(\mu\text{-}OAc)_2]PF_6$ offer the potential for the investigation of the positioning effect of hydrogen bonding on the phosphoester hydrolytic activity. Here, we report the asymmetric derivative of H_3L^2, H_3L^4, and their diiron complexes (see Chart 2), and discuss the detailed solid-state structural and solution spectroscopic and electrochemical studies of the homovalent Fe^{II}_2 and Fe^{III}_2 as well as the heterovalent forms, and also report the results of extensive phosphatase kinetic studies.

RESULTS AND DISCUSSION

Syntheses and Solid-State Properties. Ligands H_3L^2 and H_3L^4 were synthesized as described previously.[21,39] The dinuclear iron(II) complexes of H_3L^2 and H_3L^4 were prepared under an argon atmosphere in a glovebox by reaction with 2 equiv of iron(II) acetate in degassed methanol. After stirring the yellow solution of the complexes for 12 h at room temperature, addition of sodium hexafluorophosphate, filtration through a syringe filter and diffusion of degassed diethyl ether into the solutions, X-ray-quality green crystals of $[Fe^{II}_2(H_2L^2)(\mu\text{-}OAc)_2]PF_6$ and $[Fe^{II}_2(H_2L^4)(\mu\text{-}OAc)_2]PF_6$ were isolated. $[Fe^{II}_2(H_2L^2)(\mu\text{-}OAc)_2]PF_6$ and $[Fe^{II}_2(H_2L^4)(\mu\text{-}OAc)_2]PF_6$ were characterized and studied in the solid state and also in solution. The possibility of obtaining a heterovalent $Fe^{III}Fe^{II}$ complex of the asymmetric isomer $[Fe^{II}_2(H_2L^4)(\mu\text{-}OAc)_2]PF_6$ was also examined. Because of the air sensitivity of the reduced form of the samples, especially in solution, all procedures were undertaken strictly anaerobically.

The structures of $[Fe^{II}_2(H_2L^2)(\mu\text{-}OAc)_2]PF_6$ and $[Fe^{II}_2(H_2L^4)(\mu\text{-}OAc)_2]PF_6$ were determined by single-crystal X-ray crystallography. The structures for the complex cations are presented in Figure 1, and selected distances and valence angles are summarized in Table 1. (Table 1 also includes structural data of $[Fe^{III}Na(H_2L^4)(\mu\text{-}OAc)_2]PF_6$ discussed in more detail below.)

In contrast to the corresponding Zn^{II}_2 complexes,[39] the two Fe^{II}_2 complexes, $[Fe^{II}_2(H_2L^2)(\mu\text{-}OAc)_2]^+$ and $[Fe^{II}_2(H_2L^4)(\mu\text{-}OAc)_2]^+$, are both bridged 3-fold by two acetate coligands and the phenolate-linker of the dinucleating ligands. In addition to the three bridging ligands, the two Fe^{II} ions in $[Fe^{II}_2(H_2L^2)(\mu\text{-}OAc)_2]^+$ and $[Fe^{II}_2(H_2L^4)(\mu\text{-}OAc)_2]^+$ are coordinated by two pyridines and a tertiary amine each, forming octahedral coordination geometries.

While the Fe^{II}–N_{pyr} distances with the amide-free pyridine residues are in the range of 2.159–2.175 Å, the Fe^{II}–N_{pyr} distances in the amidated pyridine residues are significantly longer with bond distances from 2.279 Å to 2.364 Å. This is mainly due to the electron-withdrawing effect of the pivaloylamido residues and has been observed in other similar Fe^{II}_2 complexes.[40] The Fe^{II}–N_{amine} distances in the asymmetric system $[Fe^{II}_2(H_2L^4)(\mu\text{-}OAc)_2]^+$ also reflect the asymmetry with a significantly shorter Fe^{II}–N_{amine} distance in the amidated site (2.188(6) Å vs 2.270(5) Å), and this probably is due to geometric constraints and/or the hydrogen bonding network. The $Fe^{II}\cdots Fe^{II}$ distances also vary to some extent between the two complexes: in the asymmetric complex $[Fe^{II}_2(H_2L^4)(\mu\text{-}OAc)_2]^+$ ($Fe^{II}\cdots Fe^{II}$, 3.430 Å) is somewhat shorter than in $[Fe^{II}_2(H_2L^2)(\mu\text{-}OAc)_2$ (3.446 Å).

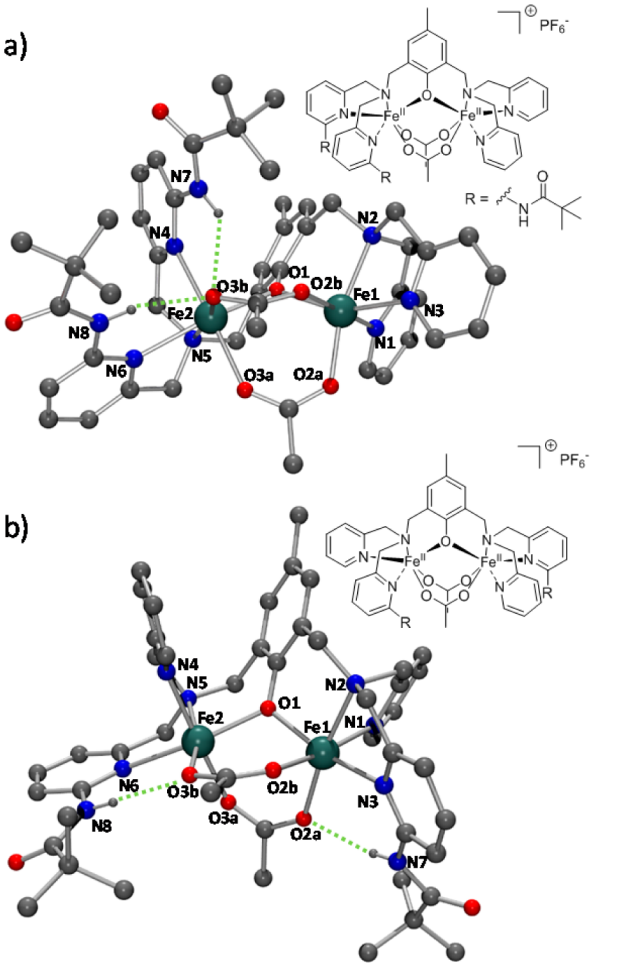

Figure 1. Structures of a) $[Fe^{II}_2(H_2L^4)(\mu\text{-}OAc)_2]^+$ and b) $[Fe^{II}_2(H_2L^2)(\mu\text{-}OAc)_2]^+$, showing hydrogen bonding (green dotted lines; counterions, noncoordinated solvent molecules and hydrogen atoms, not involved in hydrogen bonding have been omitted for clarity; ORTEP plots with 50% probability level of thermal ellipsoids are given in the Supporting Information).

When the yellow methanolic solution used for the isolation of the green crystals of $[Fe^{II}_2(H_2L^4)(\mu\text{-}OAc)_2]PF_6$ (see above) was exposed to air, the color of the solution turned immediately purple. Diffusion of diethyl ether into this solution yielded black crystals of $[Fe^{III}Na(H_2L^4)(\mu\text{-}OAc)_2]PF_6$, suitable for X-ray diffraction (XRD) analysis. The molecular cation is depicted in Figure 2, and selected distances and valence angles are presented in Table 1. The complex cation contains the deprotonated phenolate backbone, the Fe^{III} center in the amide-free binding site, a sodium ion coordinated in the amidated binding pocket and two bridging acetate coligands. The two metal ions are bridged 3-fold as in $[Fe^{II}_2(H_2L^4)(\mu\text{-}OAc)_2]^+$. The synthesis of this unprededented heterodinuclear complex with the unusual coordination of a sodium ion by the phenolate-based ligand H_3L^4 is fully reproducible.

The Fe^{III} center in $[Fe^{III}Na(H_2L^4)(\mu\text{-}OAc)_2]^+$ is coordinated similarly to the two Fe^{II} centers in $[Fe^{II}_2(H_2L^4)(\mu\text{-}OAc)_2]^+$, forming a distorted octahedral coordination geometry with two

DOI: 10.1021/acs.inorgchem.5b00628
Inorg. Chem. XXXX, XXX, XXX–XXX

Table 1. Selected Bond Lengths and Bond Angles for $[Fe^{II}_2(H_2L^2)(\mu\text{-}OAc)_2]PF_6$, $[Fe^{II}_2(H_2L^4)(\mu\text{-}OAc)_2]PF_6$, and $[Fe^{III}Na(H_2L^4)(\mu\text{-}OAc)_2]PF_6$

	$[Fe^{II}_2(H_2L^2)(\mu\text{-}OAc)_2]^+$	$[Fe^{II}_2(H_2L^4)(\mu\text{-}OAc)_2]^+$	$[Fe^{III}Na(H_2L^4)(\mu\text{-}OAc)_2]^+$
Bond Lengths (Å)			
Fe···M[a]	3.4457(3)	3.430	3.4802(6)
Fe–O(1)[b]	2.0746(13)	2.039(4)	1.8906(11)
Fe–O(2A)[b]	2.0930(13)	2.024(4)	1.9620(11)
Fe–O(2B)[b]	2.0712(13)	2.185(4)	1.9556(11)
Fe–N(1)[b]	2.1753(16)	2.167(5)	2.1702(13)
Fe–N(2)[b]	2.2311(15)	2.270(5)	2.2130(13)
Fe–N(3)[b]	2.3638(15)	2.159(5)	2.1767(13)
M–O(1)[a]	2.0378(13)	2.040(4)	2.3710(12)
M–O(3A)[a]	2.1184(14)	2.204(4)	2.3578(13)
M–O(3B)[a]	2.1020(14)	2.079(4)	2.3575(13)
M–N(4)[a]	2.1703(16)	2.290(6)	2.5819(14)
M–N(5)[a]	2.2270(16)	2.188(6)	2.4845(14)
M–N(6)[a]	2.2786(15)	2.311(5)	2.5862(15)
Bond Angles (deg)			
Fe–O(1)–M[a,b]	113.83(6)	114.45(18)	108.98(5)
O(1)–Fe–N(1)[b]	87.69(6)	91.16(18)	87.54(5)
O(1)–Fe–N(2)[b]	86.53(5)	86.17(17)	91.54(5)
O(1)–Fe–N(3)[b]	160.48(5)	156.49(19)	166.43(5)
O(1)–Fe–O(2A)[b]	102.08(5)	104.69(17)	98.85(5)
O(1)–Fe–O(2B)[b]	90.73(5)	87.79(17)	101.88(5)
O(1)–M–N(4)[a]	90.36(5)	87.09(18)	121.84(5)
O(1)–M–N(5)[a]	88.88(6)	87.69(18)	79.69(4)
O(1)–M–N(6)[a]	160.55(6)	162.03(18)	133.73(5)
O(1)–M–O(3A)[a]	89.27(6)	93.65(16)	85.18(4)
O(1)–M–O(3B)[a]	97.90(5)	103.30(16)	91.86(4)

[a]M is Na in $[Fe^{III}Na(H_2L^4)(\mu\text{-}OAc)_2]^+$ and Fe(2) in $[Fe^{II}_2(H_2L^4)(\mu\text{-}OAc)_2]^+$ and $[Fe^{II}_2(H_2L^2)(\mu\text{-}OAc)_2]^+$; O(3A) is O(2B) in $[Fe^{III}Na(H_2L^4)(\mu\text{-}OAc)_2]^+$. [b]Fe is Fe(1) in $[Fe^{II}_2(H_2L^4)(\mu\text{-}OAc)_2]^+$ and $[Fe^{II}_2(H_2L^2)(\mu\text{-}OAc)_2]^+$; O(2B) is O(3A) in $[Fe^{III}Na(H_2L^4)(\mu\text{-}OAc)_2]^+$.

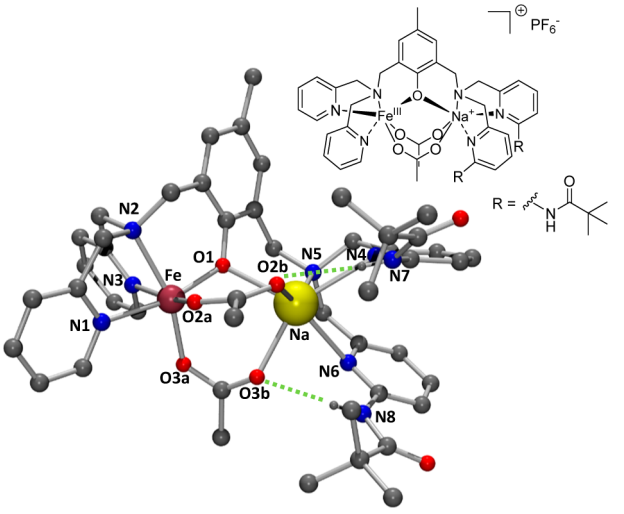

Figure 2. Structure of $[Fe^{III}Na(H_2L^4)(\mu\text{-}OAc)_2]^+$ showing hydrogen bonding (green dotted lines; counterions and hydrogen atoms, not involved in H-bonding, have been omitted for clarity; an ORTEP plot with 50% probability level of thermal ellipsoids is given in the Supporting Information).

pyridines, a tertiary amine, the bridging phenolate, and two bridging acetates. The distances of Fe^{III} to the pyridine nitrogen atoms in $[Fe^{III}Na(H_2L^4)(\mu\text{-}OAc)_2]^+$ are slightly longer than those in $[Fe^{II}_2(H_2L^4)(\mu\text{-}OAc)_2]^+$, while the bond between the Fe^{III} center and the amine nitrogen donor is shortened by 0.057 Å. More importantly, the oxidation of Fe^{II} to Fe^{III} leads to significant differences of the Fe–O (bridging acetate and phenolate) distances. Because of the higher Lewis acidity and hardness of Fe^{III}, these are shortened by 0.07–0.24 Å upon oxidation, comparable to differences observed in the hexaaqua ions $[Fe^{II}(H_2O)_6]^{2+}$ and $[Fe^{III}(H_2O)_6]^{3+}$, where Fe^{II}–OH_2 was found to be 2.13 Å and Fe^{III}–OH_2 is 2.00 Å.[41] The average Fe–O bond distance in $[Fe^{III}Na(H_2L^4)(\mu\text{-}OAc)_2]^+$ (1.94 Å) is also comparable to that found in the Fe^{III} center of $[Fe^{III}Fe^{II}(BPMP)(\mu\text{-}OPr)_2]^+$ (HBPMP = 2,6-bis[bis(pyridin-2-ylmethylamino)-methyl]-4-methylphenol, 1.96 Å), while the average Fe^{II}–O bond length in $[Fe^{III}Fe^{II}(BPMP)(\mu\text{-}OPr)_2]^+$ is 2.09 Å, close to that in $[Fe^{II}_2(H_2L^4)(\mu\text{-}OAc)_2]^+$ (2.083 and 2.108 Å).[28] Note that the bridging acetates are asymmetric in both $[Fe^{II}_2(H_2L^4)(\mu\text{-}OAc)_2]^+$ and $[Fe^{III}Na(H_2L^4)(\mu\text{-}OAc)_2]^+$, and this may also influence the average Fe^{II}–O and Fe^{III}–O distances.

The Na^+ ion in $[Fe^{III}Na(H_2L^4)(\mu\text{-}OAc)_2]^+$ has the same primary coordination sphere as the Fe^{III} center but in a trigonal prismatic geometry. As expected (charge, ionic radii), the distances of the donor groups to Na^+ are generally longer by at least 0.15 Å than the corresponding distances to Fe^{II} in $[Fe^{II}_2(H_2L^4)(\mu\text{-}OAc)_2]^+$. Consequently, the separation between the two metal centers in $[Fe^{III}Na(H_2L^4)(\mu\text{-}OAc)_2]^+$ is larger than in the Fe^{II}_2 analogue.

The structure of $[Fe^{III}Na(H_2L^4)(\mu\text{-}OAc)_2]PF_6$ suggests that the crystallization of the $Fe^{III}Na^+$ form of the complex is more likely than of the corresponding Fe^{III}_2 complex. It appears that oxidation of the two Fe^{II} centers of $[Fe^{II}_2(H_2L^4)(\mu\text{-}OAc)_2]^+$ by air produces a complex where only the Fe^{III} center in the less sterically demanding binding site remains coordinated, while the more sterically hindered binding site exchanges the metal center from Fe^{III} to Na^+ prior to crystallization.

Variable-temperature dc magnetic susceptibility data sets of finely ground crystals of $[Fe^{II}_2(H_2L^4)(\mu\text{-}OAc)_2]PF_6$ and $[Fe^{III}Na(H_2L^4)(\mu\text{-}OAc)_2]PF_6$ in the temperature range of 2–300 K were measured. The $\chi_M T$ vs T curves obtained for a powdered sample of $[Fe^{II}_2(H_2L^4)(\mu\text{-}OAc)_2]PF_6$ is reproduced in Figure 3. At 300 K, the $\chi_M T$ value of $[Fe^{II}_2(H_2L^4)(\mu$-

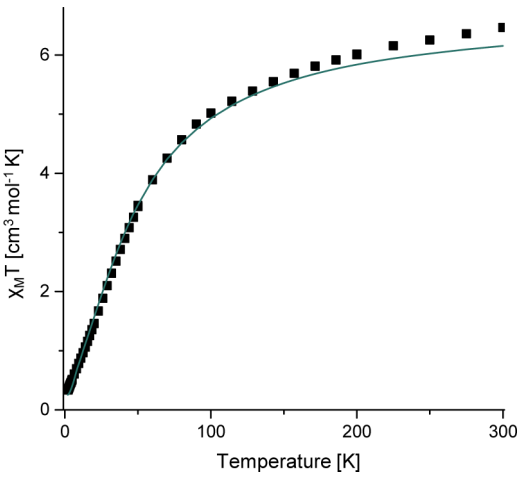

Figure 3. Temperature dependence of $\chi_M T$ for $[Fe^{II}_2(H_2L^4)(\mu\text{-}OAc)_2]PF_6$ recorded in a magnetic field of 1000 Oe and the respective fit curve (green line).

DOI: 10.1021/acs.inorgchem.5b00628
Inorg. Chem. XXXX, XXX, XXX–XXX

$OAc)_2]PF_6$ is 6.47 $cm^3\ mol^{-1}\ K$ ($\mu_{eff} = 7.19\mu_B$). This is slightly above 6.00 $cm^3\ mol^{-1}\ K$ ($\mu_{eff} = 6.93\mu_B$), the value expected for two noninteracting *high-spin* Fe^{II} ions. The continuous decrease of $\chi_M T$ with decreasing temperature suggests antiferromagnetic coupling between the two Fe^{II} centers in $[Fe^{II}_2(H_2L^4)(\mu\text{-}OAc)_2]PF_6$. This is confirmed by $\chi_M T = 0.35\ cm^3\ mol^{-1}\ K$ ($\mu_{eff} = 1.35\mu_B$) below 2 K, indicating an $S = 0$ ground state for $[Fe^{II}_2(H_2L^4)(\mu\text{-}OAc)_2]PF_6$. A small proportion (~5%) of the paramagnetic monoiron(III) complex is suggested to account for the slightly higher than expected experimental $\chi_M T$ values.

The data were fitted to a simplified van Vleck formula for two interacting $S = 2$ spins, derived from the Heisenberg Hamiltonian (eq 1) and including a correction for paramagnetic impurities (eq 2).[42]

$$H = -2JS_1S_2 \tag{1}$$

$$\chi_M = \left[\frac{N_A g^2 \mu_B{}^2}{3kT}(S_T(S_T+1))\right]p + \frac{N_A g^2 \mu_B{}^2}{3kT}(S(S+1)(1-p)) \tag{2}$$

Here, N_A is Avogadro's number, g the Landé factor, μ_B the Bohr magneton, k the Boltzmann constant, J the interaction parameter, S_T the total spin, and S the electron spin of the impurity p.

The best fit, shown in Figure 3, was obtained with $J = -5.05\ cm^{-1}$ with fixed value of $g = 2.15$, in agreement with antiferromagnetic coupling, and 5.8% monoiron(III) paramagnetic impurity ($S = 5/2$). The weak antiferromagnetic exchange is as expected from published data ($-5\ cm^{-1} > J > -11\ cm^{-1}$) of similar PAP model systems,[43−45] and it appears that J is correlated to the Fe^{II}−(μ-O) distance and the Fe^{II}−O−Fe^{II} angle.[43,45]

For the monoiron(III) complex $[Fe^{III}Na(H_2L^4)(\mu\text{-}OAc)_2]PF_6$ at 300 K, $\chi_M T = 4.29\ cm^3\ mol^{-1}\ K$ ($\mu_{eff} = 5.84\mu_B$). This is close to the expected value for five unpaired electrons ($\chi_M T = 4.39\ cm^3\ mol^{-1}\ K$, $\mu_{eff} = 5.92\mu_B$).

Solution Properties. *(i). Electrochemistry.* The electrochemical behavior of $[Fe^{II}_2(H_2L^4)(\mu\text{-}OAc)_2]^+$ was investigated by cyclic voltammetry (CV) in degassed acetonitrile solution (0.1 M NBu_4ClO_4, 0.5 mM complex) at room temperature, with a glassy carbon working electrode, a platinum wire as a counter electrode and a Ag/Ag^+ (0.1 mM in NaCl) reference electrode. Ferrocene was used as an internal standard and the redox potentials are reported vs SCE (Fc/Fc^+) = 0.380 V vs SCE).[46] CV scans were essentially identical when the experiments were undertaken multiple times under anaerobic conditions, indicating that substantial decomposition in solution does not occur. A typical CV is shown in Figure 4.

The CV of $[Fe^{II}_2(H_2L^4)(\mu\text{-}OAc)_2]PF_6$ shows two sequential oxidations: a reversible one-electron transfer at 0.16 V vs SCE ($\Delta E_P = 88$ mV) and a quasi-reversible one-electron transfer at 0.56 V vs SCE ($\Delta E_P = 153$ mV) (Figure 4a), assigned to the $Fe^{II}_2/Fe^{III}Fe^{II}$ and $Fe^{III}Fe^{II}/Fe^{III}_2$ couples, respectively. Table 2 compares these redox potentials with relevant literature data (HBPLMP = 2,6-bis[((2-pyridylmethyl)(6-methyl-2-pyridylmethyl)amino)-methyl]-4-methylphenol). Interestingly, with $[Fe^{II}_2(H_2L^4)(\mu\text{-}OAc)_2]PF_6$ E_1 is shifted to more positive and E_2 to more negative potentials, with respect to the complexes of the nonsubstituted HBPMP ligand. A shift to more positive potentials by substitution with pivaloylamide groups was described previously, and the decreased charge of the hydroxamate oxygen due to hydrogen bonding was proposed to be responsible for the observed preference for

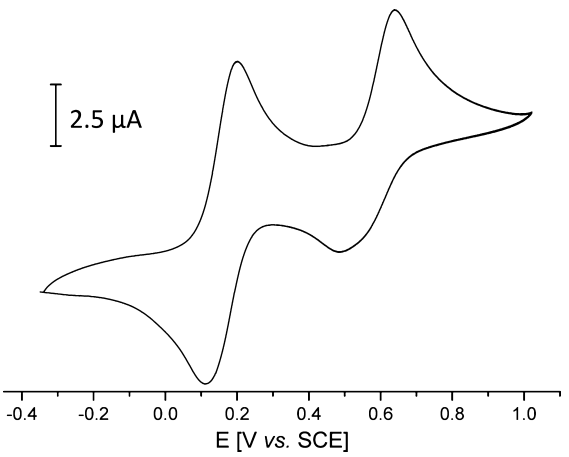

Figure 4. Cyclic voltammogram of $[Fe^{II}_2(H_2L^4)(\mu\text{-}OAc)_2]PF_6$, recorded in acetonitrile with 0.1 M NBu_4ClO_4 under Ar vs Ag/AgCl (starting potential: −0.42 V; initial direction: positive).

the reduced form.[47,48] The air-oxidized solution of the diiron complex of H_3L^4 was also studied by CV and indicates that severe structural changes occurred upon air oxidation, leading to irreversible redox processes (see the Supporting Information).

One of the objectives of ligand modification is to stabilize the mixed-valence $Fe^{III}Fe^{II}$ form of the PAP model complexes. Therefore, the relative stabilitiy of the $Fe^{III}Fe^{II}$ complex of the asymmetric ligand H_3L^4 was estimated by examining the comproportionation equilibrium defined in eq 3:

$$[Fe^{II}_2(H_2L^+)(OAc)_2]^+ + [Fe^{III}_2(H_2L^+)(OAc)_2]^{3+} \overset{K_{com}}{\rightleftharpoons} 2[Fe^{III}Fe^{II}(H_2L^4)(OAc)_2]^{2+} \tag{3}$$

From the separation of the redox potentials ΔE, the comproportionation constant K_{com} can be calculated by eq 4,

$$\Delta E = \left(\frac{RT}{nF}\right)\ln K_{com} \tag{4}$$

($n = 1$), and the corresponding values are also listed in Table 2. The small value of ΔE for $[Fe^{II}_2(H_2L^4)(\mu\text{-}OAc)_2]^+$ (0.41 V) yielded $K_{com} = 8.5 \times 10^6$, indicating substantial stability of the $Fe^{III}Fe^{II}$ mixed valent complex. However, the comproportionation constant is much smaller than those reported for other phenoxido-bridged diiron complexes (see Table 2).

(ii). ^{1}H NMR Spectroscopy. ^{1}H NMR spectroscopy was used to probe the symmetry of the diiron(II) complexes in solution. The spectra of the paramagnetic complexes $[Fe^{II}_2(H_2L^4)(\mu\text{-}OAc)_2]PF_6$ and $[Fe^{II}_2(H_2L^2)(\mu\text{-}OAc)_2]PF_6$ (see Figure 5) have well-resolved and relatively narrow resonances, and chemical shifts of the resonances extend from −20 ppm to 200 ppm, consistent with fast electronic relaxation at the *high-spin* Fe^{II} centers, because of their energetically low-lying excited states.[50]

Comparison of the spectra of the symmetric and asymmetric isomers based on H_3L^2 and H_3L^4, respectively, suggest that the symmetry provided by the ligands is still present in the corresponding diiron(II) complexes: in the spectrum recorded from $[Fe^{II}_2(H_2L^2)(\mu\text{-}OAc)_2]^+$, 18 resonances are observed; in the spectrum of $[Fe^{II}_2(H_2L^4)(\mu\text{-}OAc)_2]^+$, there are 32 resonances (i.e., one resonance for each proton). In the case of $[Fe^{II}_2(H_2L^2)(\mu\text{-}OAc)_2]^+$, because of a rotation axis, two protons each resonate at similar fields and, therefore, there was one resonance for the two symmetry-related protons observed.

DOI: 10.1021/acs.inorgchem.5b00628
Inorg. Chem. XXXX, XXX, XXX−XXX

Table 2. Cyclic Voltammetric Data of Phenoxido-bridged Diiron Complexes

complex	ref	E_1 [V vs SCE]	E_2 [V vs SCE]	ΔE [V]	K_{com}
$[Fe^{II}_2(H_2L^4)(\mu\text{-}OAc)_2]PF_6$		0.16	0.56	0.41	8.5×10^6
$[Fe^{III}Fe^{II}(BPMP)(\mu\text{-}OAc)_2](BF_4)_2$	29	−0.03	0.68	0.71	1.6×10^{12}
$[Fe^{III}Fe^{II}(BPMP)(\mu\text{-}OPr)_2](BPh_4)_2$	28	−0.01	0.69	0.70	7.5×10^{11}
$[Fe^{III}Fe^{II}(BPMP)(\mu\text{-}OBz)_2](PF_6)_2$	28	0.06	0.75	0.69	4.7×10^{11}
$[Fe^{III}Fe^{II}(BPMP)(\mu\text{-}OBz)_2](BF_4)_2$	29	0.05	0.73	0.68	5.0×10^{11}
$[Fe^{III}Fe^{II}(BPMP)(\mu\text{-}OBz)_2](BF_4)_2$	49	−0.02	0.67	0.69	6.8×10^{11}
$[Fe^{III}Fe^{II}(BPLMP)(\mu\text{-}OAc)_2](BPh_4)_2$	30	−0.09	0.66	0.75	3.3×10^{12}

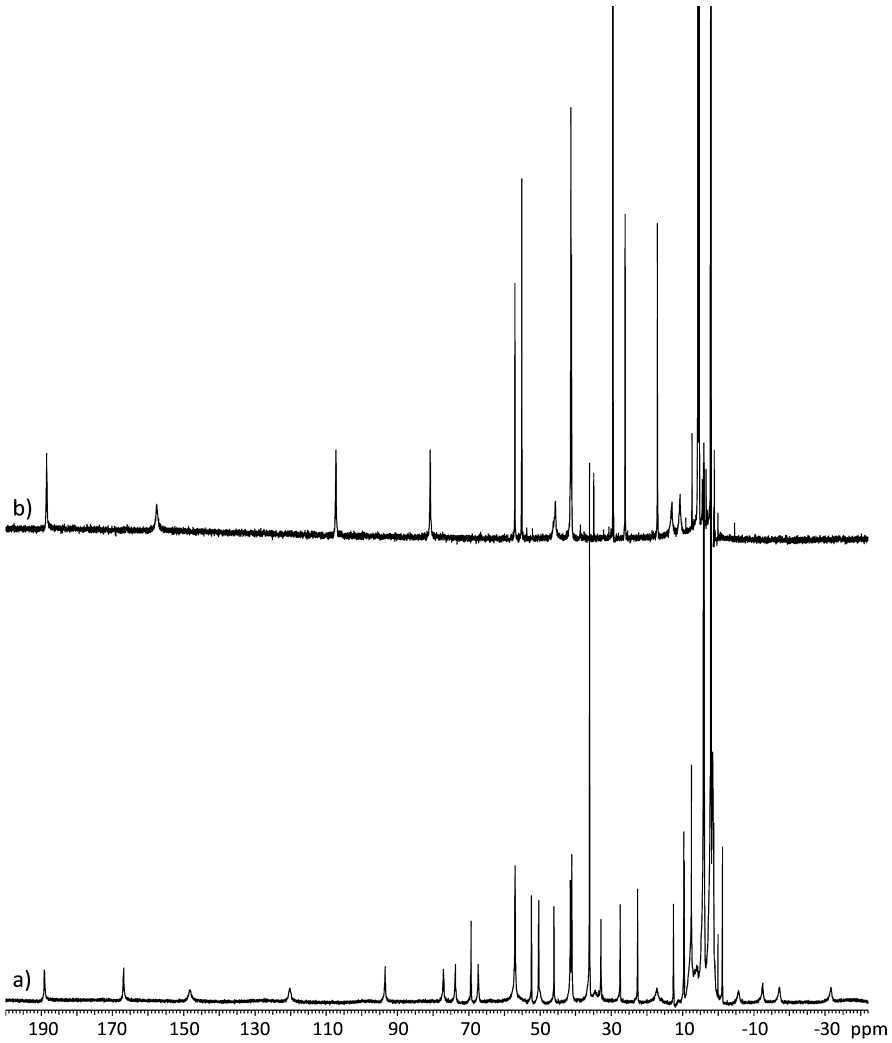

Figure 5. ^{1}H NMR spectrum of (a) $[Fe^{II}_2(H_2L^4)(\mu\text{-}OAc)_2]PF_6$ and (b) $[Fe^{II}_2(H_2L^2)(\mu\text{-}OAc)_2]PF_6$ in CD_3CN.

Moreover, the spectrum of $[Fe^{II}_2(H_2L^4)(\mu\text{-}OAc)_2]^+$ exhibits two equally intense sharp resonances at 3.86 and 4.08 ppm; based on the integration for nine protons, these resonances are assigned to the two *tert*-butyl groups of the pivaloylamide residues. In contrast, the spectrum of $[Fe^{II}_2(H_2L^2)(\mu\text{-}OAc)_2]^+$ shows a resonance integrating for 18 protons at 5.40 ppm.

The magnetic properties of $[Fe^{II}_2(H_2L^4)(\mu\text{-}OAc)_2]^+$ were also investigated by NMR spectroscopy.[51] In solution, the complex exhibits an effective magnetic moment of $6.10\mu_B$ This is lower than the calculated spin-only value for two non-interacting *high-spin* Fe^{II} centers ($\mu_{eff} = 6.93\mu_B$), indicating the presence of exchange coupling between the two metal centers. Note that the solution magnetic moment is somewhat different from that in the solid state (see above), indicating some structural change upon dissolution of the solid.

(iii). Mass Spectrometry. ESI^+ mass spectrometry of $[Fe^{II}_2(H_2L^4)(\mu\text{-}OAc)_2]PF_6$ in dichloromethane results in a spectrum with a main peak at 924.36 m/z and two smaller peaks at 889.24 m/z and 957.31 m/z, with isotopic patterns characteristic for diiron complexes (Figure 6). The signals are assigned to $[Fe^{II}_2(L^4)(CH_3CH_2OH)(CH_3CN)]^+$, $[Fe^{II}_2(HL^4)\text{-}(CH_3OH)F]^+$ (the fluoride co-ligand may derive from the hydrolysis of PF_6^- observed previously)[52−55] and the intact complex $[Fe^{II}_2(H_2L^4)(OAc)_2]^+$, respectively. When the acetonitrile solution of $[Fe^{II}_2(H_2L^4)(\mu\text{-}OAc)_2]PF_6$ was exposed to air for ∼10 min prior to the measurement, one main signal was

DOI: 10.1021/acs.inorgchem.5b00628
Inorg. Chem. XXXX, XXX, XXX−XXX

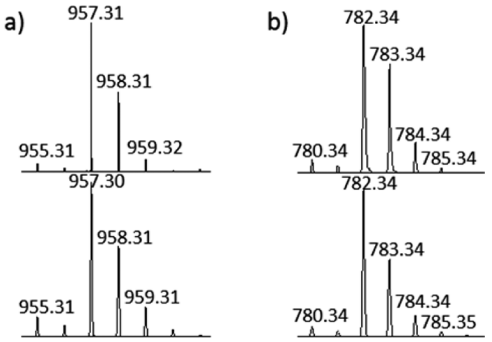

Figure 6. Characteristic isotopic pattern found in ESI^+ mass spectrometry (experimental, top and calculated, bottom) of $[Fe^{II}_2(H_2L^4)(\mu\text{-}OAc)_2]PF_6$ (a) in dichloromethane and immediate measurement ($[Fe^{II}_2(H_2L^4)(OAc)_2]^+$) and (b) in acetonitrile after exposure to air for ~10 min ($[Fe(HL^4)]^+$).

detected at 782.3 m/z, assigned to the monoiron(III) complex $[Fe^{III}(HL^4)]^+$.

The solubility of $[Fe^{II}_2(H_2L^2)(\mu\text{-}OAc)_2]PF_6$ in dichloromethane was lower than that of $[Fe^{II}_2(H_2L^4)(\mu\text{-}OAc)_2]PF_6$ and made the addition of methanol necessary. The resulting spectrum exhibited a main signal at 729.42 m/z, matching the protonated ligand $[H_4L^2]^+$ and an intense signal at 782.34 m/z for the oxidation product $[Fe^{III}(HL^2)]^+$. This result suggests that the mass spectrometric investigation of the Fe^{II}_2 complex in solution is hampered by fast oxidation. However, signals with the characteristic diiron isotopic pattern were observed at 929.28 m/z, 943.29 m/z, and 957.31 m/z, and these are assigned to the diiron species $[Fe^{II}_2(H_2L^2)(OAc)(CH_3O)]^+$, $[Fe^{II}_2(H_2L^2)(OAc)(CH_3CH_2O)]^+$, and the intact complex $[Fe^{II}_2(H_2L^2)(OAc)_2]^+$ (see Supporting Information for the spectra).

The ESI^+ mass spectrometric investigations of the purple solid $[Fe^{III}Na(H_2L^4)(\mu\text{-}OAc)_2]PF_6$, dissolved in methanol, resulted in a spectrum with a main peak at 872.37 m/z, assigned to $[Fe^{III}(H_2L^4)(CH_3OH)(OAc)]^+$ (see Supporting Information for the spectra).

(iv). Ultraviolet–Visible–Near-Infrared (UV-vis-NIR) Spectroscopy. In addition to the intense absorptions below 300 nm (π–π^* transitions of the ligand backbone), the electronic spectra of acetonitrile solutions of $[Fe^{II}_2(H_2L^2)(\mu\text{-}OAc)_2]^+$ and $[Fe^{II}_2(H_2L^4)(\mu\text{-}OAc)_2]^+$ show only one transition in the region of 400–450 nm. $[Fe^{II}_2(H_2L^4)(\mu\text{-}OAc)_2]^+$ exhibits an electronic spectrum with a band at 416 nm (ε = 1446 M^{-1} cm^{-1}), and $[Fe^{II}_2(H_2L^2)(\mu\text{-}OAc)_2]^+$ has a transition at 409 nm (ε = 1315 M^{-1} cm^{-1}), ascribed to an MLCT transition of Fe^{II} to pyridine nitrogen atoms. This is in accord with previously published Fe^{II}_2 complexes.[28,40,56,57] The lack of low-energy visible absorption bands, despite the presence of pyridine ligands, indicates that $[Fe^{II}_2(H_2L^4)(\mu\text{-}OAc)_2]^+$ and $[Fe^{II}_2(H_2L^2)(\mu\text{-}OAc)_2]^+$ are *high-spin* Fe^{II} complexes.[57]

The UV-vis-NIR spectrum of an acetonitrile solution of $[Fe^{III}Na(H_2L^4)(\mu\text{-}OAc)_2]^+$ shows one broad transition at 568 nm (ε = 2500 M^{-1} cm^{-1}) and a shoulder at 335 nm (ε = 5050 M^{-1} cm^{-1}), in addition to the intense absorptions below 300 nm. The band at 568 nm is associated with the phenolate-to-iron(III) charge transfer (CT) transition from the O p_π to the Fe^{III} d_{π^*} orbitals and is energetically close to the tyrosinate-to-iron(III) charge transfer observed for PAPs.[6−10] The majority of synthetic Fe^{III}-phenolate complexes exhibit CT bands with

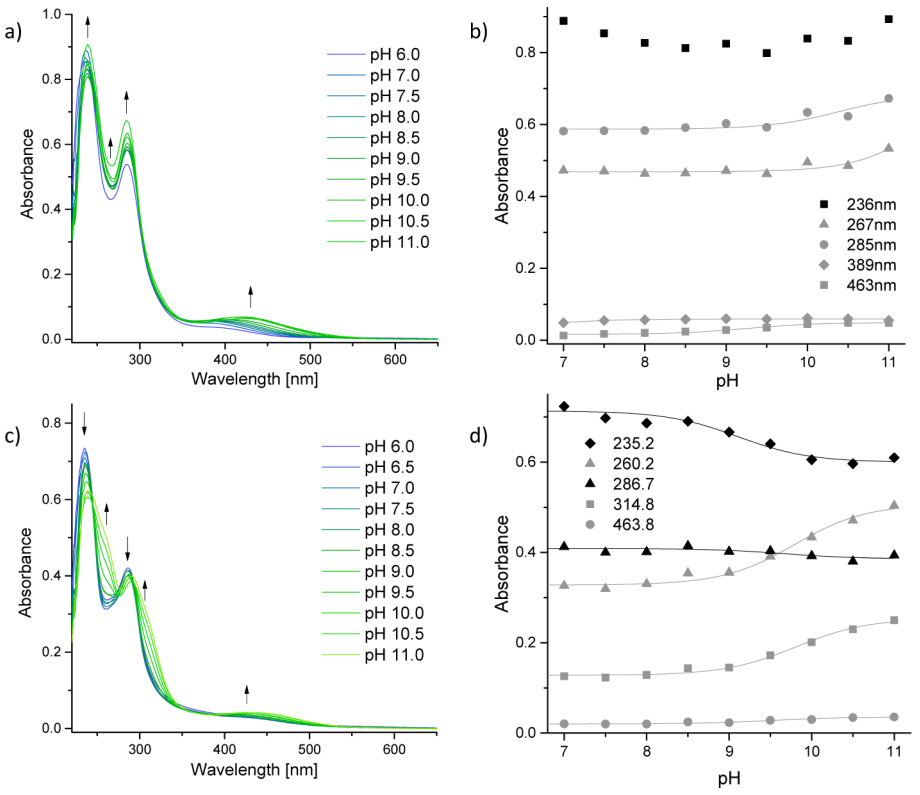

Figure 7. UV-vis spectroscopic titration (50 μM in acetonitrile/buffer between pH 6 and 11) and absorbance vs pH plots for (a and b) $[Fe^{II}_2(H_2L^4)(\mu\text{-}OAc)_2]PF_6$ and (c and d) $[Fe^{II}_2(H_2L^2)(\mu\text{-}OAc)_2]PF_6$. The solid lines in panels b and d correspond to fitted curves using eq S6 in the Supporting Information.

DOI: 10.1021/acs.inorgchem.5b00628
Inorg. Chem. XXXX, XXX, XXX–XXX

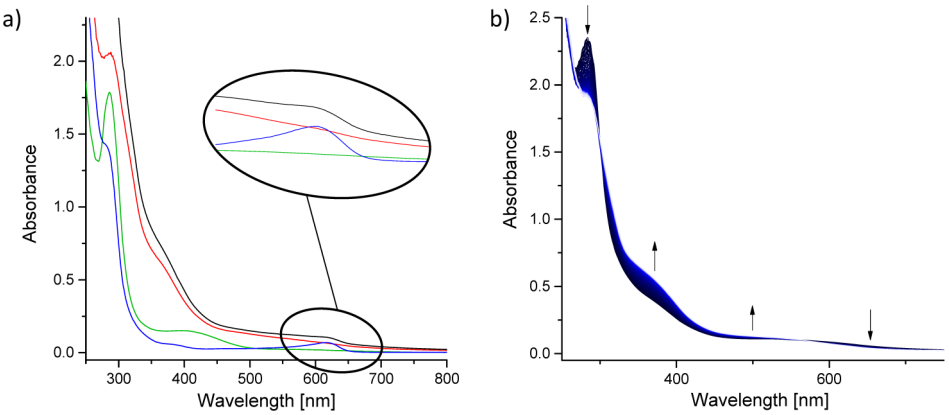

Figure 8. UV-vis-NIR spectra during addition of ferrocenium hexafluorophosphate (blue line) to (a) $[Fe^{II}_2(H_2L^4)(\mu\text{-}OAc)_2]PF_6$ (green line, without $Fe^{III}Cp_2PF_6$; red line, 1 equiv $Fe^{III}Cp_2PF_6$; black line, 2 equiv $Fe^{III}Cp_2PF_6$) and (b) time-dependent experiments of $[Fe^{II}_2(H_2L^4)(\mu\text{-}OAc)_2]PF_6$ with 1 equiv $Fe^{III}Cp_2PF_6$.

molar extinction coefficients of the order of 1000−2000 M^{-1} cm^{-1} per Fe^{III}-phenolate bond.[58,59] The molar extinction coefficient of 2500 M^{-1} cm^{-1} of $[Fe^{III}Na(H_2L^4)(\mu\text{-}OAc)_2]^+$ is outside this range but does not approach the value found for the native enzymes.[6−10] Comparison with a variety of similar doubly acetate bridged $Fe^{III}M^{II}$ complexes of H_2BPBPMP reveals that the molar extinction coefficient is strongly dependent on the nature of the M^{II} ion.[34]

In order to examine the behavior of $[Fe^{II}_2(H_2L^4)(\mu\text{-}OAc)_2]^+$ and $[Fe^{II}_2(H_2L^2)(\mu\text{-}OAc)_2]^+$ under basic conditions, UV-vis-NIR spectra were also recorded in acetonitrile-aqueous buffer mixtures (1:1). The pH of the aqueous buffer was varied from 6 to 11 (the pH refers to the aqueous component). With increasing basicity, the absorbance spectrum of $[Fe^{II}_2(H_2L^2)(\mu\text{-}OAc)_2]^+$ (Figure 7c) shows a decrease in intensity of the two bands at 235 and 286 nm, while two new bands arise at 261 and 314 nm. Moreover, the band at 414 nm experiences a shift to 440 nm with increasing basicity. Figure 7d shows the change of absorbance at different wavelengths as a function of rising pH. The overlay of the spectra at different pH values indicates the presence of three isosbestic points at 245 nm, 274 nm, and 395 nm. This indicates that the diiron(II) complex is stable in the pH range investigated and undergoes a single deprotonation step. Therefore, the data can be analyzed with the Henderson−Hasselbalch equation (see the Supporting Information for details), and a pK_a value of 9.58 ± 0.65 emerges for $[Fe^{II}_2(H_2L^2)(\mu\text{-}OAc)_2]^+$. This is ∼1.5 pH units higher than that observed with the corresponding dizinc(II) complex, i.e., following the same trend as the corresponding metal aqua complexes.[60] Therefore, the pK_a value is assigned to the deprotonation of a Fe^{II}-bound water molecule.

pH-dependent UV-vis-NIR spectroscopy of $[Fe^{II}_2(H_2L^4)(\mu\text{-}OAc)_2]^+$ show a similar shift of the band at 399 nm to 426 nm (Figure 7a). In contrast to $[Fe^{II}_2(H_2L^2)(\mu\text{-}OAc)_2]^+$, both transitions in the region of 200−300 nm in the spectrum of $[Fe^{II}_2(H_2L^4)(\mu\text{-}OAc)_2]^+$ increase in intensity with increasing basicity. The absorbance vs pH plot (Figure 7b) exhibits changes in the pH regions around 7 and 10.5, indicating two deprotonation steps with pK_a values of ∼7 and 10.5.

(v). Mössbauer Spectroscopy. In order to investigate the coordination chemistry of the two Fe^{II} centers in $[Fe^{II}_2(H_2L^4)(\mu\text{-}OAc)_2]PF_6$, a ^{57}Fe enriched sample was prepared, and a ^{57}Fe Mössbauer spectrum was measured in frozen acetonitrile solution at 170 K (see the next section). The spectrum obtained shows a single quadrupole doublet, indicating similar electronic environments for both Fe^{II} centers. The parameters determined by fitting the spectrum with NORMOS,[61] leading to δ = 1.13(1) mm/s and ΔE_Q = 2.66(1) mm/s (Γ = 0.45(1) mm/s), are consistent with Fe^{II} in a *high-spin* electronic configuration and in agreement with values reported for other similar dinuclear *high-spin* Fe^{II} complexes.[62]

(vi). Formation of a Heterovalent $Fe^{III}Fe^{II}$ Complex. The presence of a heterovalent diiron core and the hydrogen bonding network due to the protein backbone are essential features of the PAP active site. Therefore, the generation of a $Fe^{III}Fe^{II}$ complex of H_3L^4 was expected to create an accurate structural, spectroscopic and functional model for PAP. In order to generate $[Fe^{III}Fe^{II}(H_2L^4)(solv)_x]^{4+}$ the chemical oxidation was followed by electronic spectroscopy, and the putative model compound was then examined with ^{57}Fe Mössbauer and EPR spectroscopy. The formation of a heterovalent diiron complex of the symmetric ligand H_3L^2 by bulk electrolysis was investigated previously with the same techniques.[21]

(a). UV-vis-NIR Spectroscopy. Because of two well-separated redox waves in the cyclic voltammogram (CV) of $[Fe^{II}_2(H_2L^4)(\mu\text{-}OAc)_2]^+$, with potentials above and below (0.16 V, 0.56 V) that of ferrocene (0.38 V), the chemical oxidation of $[Fe^{II}_2(H_2L^4)(\mu\text{-}OAc)_2]^+$ was examined using ferrocenium hexafluorophosphate as an oxidant. Therefore, a solution of $[Fe^{II}_2(H_2L^4)(\mu\text{-}OAc)_2]^+$ in acetonitrile was treated with 1 and 2 equiv of ferrocenium hexafluorophosphate under anaerobic conditions. The mixtures were allowed to react for 12 h. From the UV-vis-NIR spectra (see Figure 8), it is apparent that the oxidant reacts with the diiron(II) complex in the ratio of $[Fe^{II}_2(H_2L^4)(\mu\text{-}OAc)_2]^+$ to ferrocenium of 1:1. UV-vis transitions at 362 nm (ε = 6360 M^{-1} cm^{-1}) and 500 nm (ε = 1270 M^{-1} cm^{-1}) appear, while the bands at 283 and 654 nm decrease (Figure 8b). Further addition of ferrocenium hexafluorophosphate to a ratio of $[Fe^{II}_2(H_2L^4)(\mu\text{-}OAc)_2]^+$ to ferrocenium of 1:2 results in a similar UV-vis spectrum (362 nm, ε = 7460 M^{-1} cm^{-1} and 500 nm, ε = 1470 M^{-1} cm^{-1}), except for an additional shoulder at 619 nm. This shoulder is due to unreacted ferrocenium hexafluorophosphate and indicates that the oxidant is not able to oxidize both Fe^{II} ions of $[Fe^{II}_2(H_2L^4)(\mu\text{-}OAc)_2]^+$. This supports the selective formation of the heterovalent complex $[Fe^{III}Fe^{II}(H_2L^4)(solv)_x]^{4+}$. Note that the loss of acetate bridges, in particular

DOI: 10.1021/acs.inorgchem.5b00628
Inorg. Chem. XXXX, XXX, XXX−XXX

with heterovalent $Fe^{III}Fe^{II}$ complexes, is well-documented.[32,55,63,64]

(b). Mössbauer Spectroscopy. The heterovalent form of $[Fe^{III}Fe^{II}(H_2L^4)(solv)_x]^{4+}$, generated by oxidation of $[Fe^{II}_2(H_2L^4)(\mu\text{-}OAc)_2]^+$ with ferrocenium hexafluorophosphate, was confirmed by ^{57}Fe Mössbauer spectroscopy. The mixture of ^{57}Fe-enriched $[Fe^{II}_2(H_2L^4)(\mu\text{-}OAc)_2]^+$ with 1 equiv of ferrocenium hexafluorophosphate as oxidant after 12 h at room temperature shows signals of both Fe^{III} and Fe^{II} (Figure 9b). Moreover, the presence of Fe^{III} and Fe^{II} in an equimolar ratio emerges from the 1:1 ratio of areas of the two sets of quadrupole doublets. That is, $[Fe^{III}Fe^{II}(H_2L^4)(solv)_x]^{4+}$ appears to be stable in solution. In addition, the Mössbauer parameters of the characteristic *high-spin* Fe^{III} quadrupole doublet [δ(I) = 0.41(1) mm/s and ΔE_Q(I) = 0.36(2) mm/s (Γ(I) = 0.38(1) mm/s)] and the characteristic *high-spin* Fe^{II} quadrupole doublet [δ(II) = 1.17(1) mm/s and ΔE_Q(II) = 2.78(1) mm/s (Γ(II) = 0.53(2) mm/s)] are comparable to parameters of previously reported phenolate-bridged $Fe^{III}Fe^{II}$ complexes.[33,65−67] Moreover, the ^{57}Fe Mössbauer spectrum of the asymmetric complex $[Fe^{III}Fe^{II}(H_2L^4)(solv)_x]^{4+}$ shows distinct Fe^{III} and Fe^{II} centers, i.e., these are valence-trapped, indicating that each of the metal ions is bound selectivity to one of the two binding sites.

Addition of 1 or 2 equiv of ferrocenium hexafluorophosphate to the solution of ^{57}Fe enriched $[Fe^{II}_2(H_2L^4)(\mu\text{-}OAc)_2]^+$ in acetonitrile resulted in comparable ^{57}Fe Mössbauer spectra (Figures 9b and 9c). This supports the interpretation that the oxidant cannot oxidize both Fe^{II} centers of $[Fe^{II}_2(H_2L^4)(\mu\text{-}OAc)_2]^+$; the result is the selective formation of the heterovalent $[Fe^{III}Fe^{II}(H_2L^4)(solv)_x]^{4+}$ complex.

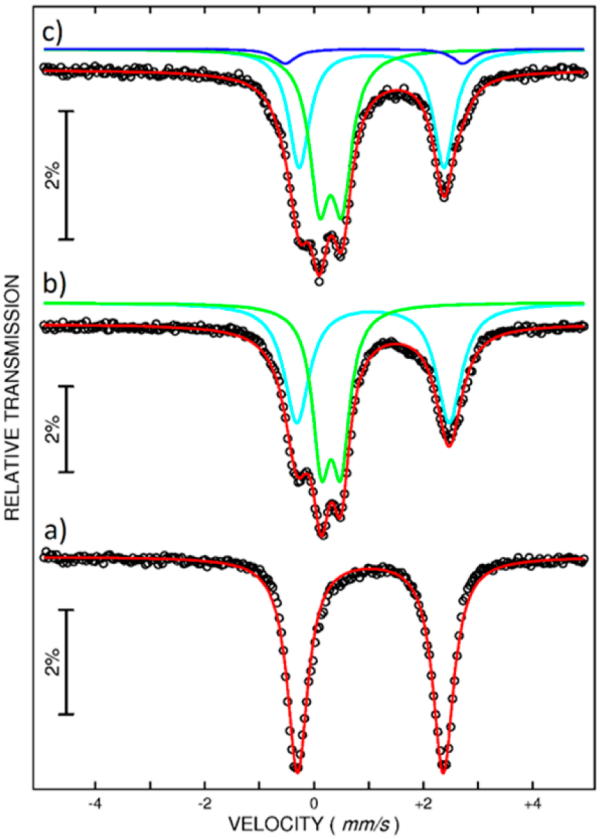

Figure 9. Comparison of ^{57}Fe Mössbauer spectra of (a) $[Fe^{II}_2(H_2L^4)(\mu\text{-}OAc)_2]PF_6$ in acetonitrile and (b) with 1 equiv of $Fe^{III}Cp_2PF_6$, and (c) with 2 equiv of $Fe^{III}Cp_2PF_6$.

(c). EPR Spectroscopy. EPR spectroscopy is generally a useful tool for the characterization of the $Fe^{III}Fe^{II}$ core in heterovalent diiron model complexes and proteins.[21] At low temperature, $Fe^{III}Fe^{II}$ complexes exhibit a broad EPR signal at $g_{av} < 2$, indicative of antiferromagnetically coupled *high-spin* Fe^{III} ($S_1 = 5/2$, ^{6}A state) and *high-spin* Fe^{II} ($S_2 = 2$, ^{5}T state), resulting in a spin ground state of $S_{total} = 1/2$. These signals are only observed near liquid helium temperature and almost disappear above 30 K.[67] Such a behavior is very similar to that of the heterovalent form in the enzymes.[67]

EPR spectra of $[Fe^{II}_2(H_2L^4)(\mu\text{-}OAc)_2]^+$ in acetonitrile, reacted with 1 or 2 equiv of ferrocenium hexafluorophosphate for 12 h, were recorded at temperatures below 5 K in order to investigate the oxidation and electronic state of the oxidized form of the model complex. The resulting spectra are presented in Figure 10. Both spectra show a broad and intense signal centered near $g = 1.6$ ($g_1 = 1.43$, $g_2 = 1.67$, $g_3 = 1.82$, derived from a fit of the spectrum, assuming an Fe^{III} ($S = 1/2$) center), in addition to a strong signal near $g = 4.3$ (the additional signal at $g = 2.04$ was shown to be an artifact due to a copper impurity in the cavity of the spectrometer). These spectra are similar to that obtained from the electrochemically generated heterovalent complex $[Fe^{III}Fe^{II}(H_2L^2)(\mu\text{-}OH)]^{3+}$.[21]

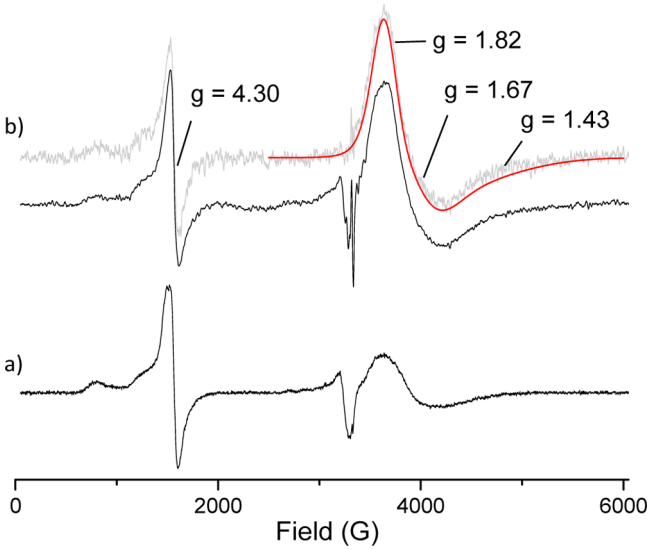

Figure 10. X-band EPR spectra of mixtures of $[Fe^{II}_2(H_2L^4)(\mu\text{-}OAc)_2]^+$ with (a) 1 equiv $Fe^{III}Cp_2PF_6$ (T = 5 K, ν = 9.37 GHz) and (b) 2 equiv of $Fe^{III}Cp_2PF_6$ (T = 1.7 K, ν = 9.37 GHz); 1 mM in acetonitrile:toluene solution (1:1), (experimental spectra shown in black, spectrum after subtraction of a copper impurity shown in gray, and simulated spectrum shown in red).

The signal at $g \approx 1.6$ is attributed to an antiferromagnetically coupled $Fe^{III}Fe^{II}$ core. Similar broad signals in this region have previously been reported for similar heterovalent model systems,[28,30,32,65,67] and bsPAP exhibits a rhombic spectrum with apparent g values of 1.58, 1.73, and 1.85 at pH > 5.[8] The fact that both mixtures show similar EPR spectra with features typical for an $Fe^{III}Fe^{II}$ species supports the proposal that ferrocenium can only oxidize one of the two Fe^{II} centers of $[Fe^{II}_2(H_2L^4)(\mu\text{-}OAc)_2]^+$.

Both frozen solution spectra exhibit a relatively sharp signal at $g_{eff} \approx 4.3$($g_{1,eff} = 4.28$, $g_{2,eff} = 5.57$, $g_{3,eff} = 9.44$). The intense

DOI: 10.1021/acs.inorgchem.5b00628
Inorg. Chem. XXXX, XXX, XXX−XXX

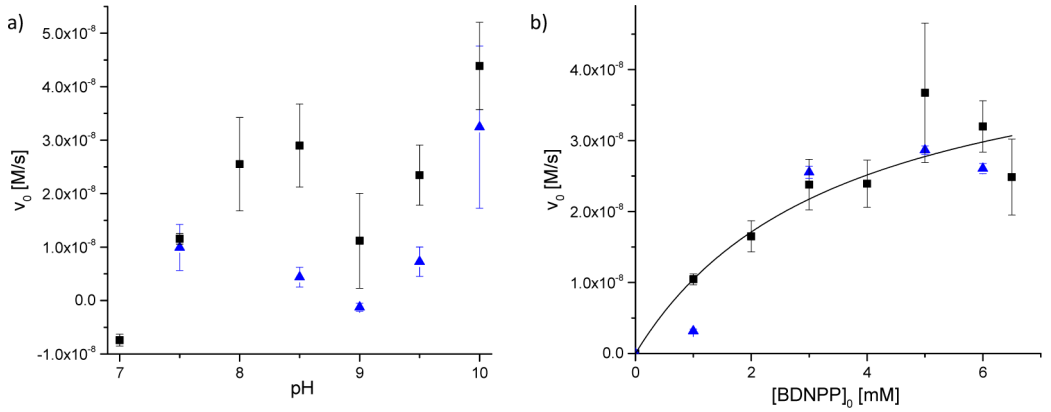

Figure 11. (a) pH dependence and (b) substrate concentration dependence at pH 9.5 of BDNPP hydrolysis activity for $[Fe^{II}_2(H_2L^4)(\mu\text{-}OAc)_2]^+$ (solid black squares) and $[Fe^{II}_2(H_2L^2)(\mu\text{-}OAc)_2]^+$ (solid blue triangles).

Table 3. Kinetic Data (k_{cat}, K_M, and k_{cat}/K_m) of BDNPP Hydrolysis for $[Fe^{II}_2(H_2L^4)(\mu\text{-}OAc)_2]^+$ and Reported Diiron Complexes (All Kinetic Studies Were Undertaken in a Mixture of Acetonitrile:Aqueous Buffer Solution (1:1)) (H_3HPBA = 2-((2-hydroxy-5-methyl-3-((pyridin-2-ylmethylamino)methyl)benzyl)(2-hydroxybenzyl)amino)acetic acid)

complex	ref	pK_a(I)	pK_a(II)	k_{cat} ($\times 10^{-3}$ s^{-1})	K_M (mM)	k_{cat}/K_M (s^{-1} M^{-1})	pH_{MM}[a]
$[Fe^{II}_2(H_2L^4)(OAc)_2]^+$		n.a.[b]	n.a.[b]	2.37 ± 0.29	3.53 ± 0.68	0.67	9.5
$[Fe^{III}_2(BPMP)(solv)_x]^{5+}$	21	5.00	7.15	0.17 ± 0.01	1.74 ± 0.35	0.10	6.35
$[Fe^{III}_4(HPBA)_2(OAc)_2(\mu\text{-}O)(\mu\text{-}OH)(OH_2)_2]^+$	69	5.42	8.41	1.6 ± 0.2	7.4 ± 0.6	0.22	6.5
$[Fe^{III}_2(H_2L^2)(solv)_x]^{5+}$	21	5.16	7.43	0.47 ± 0.03	5.92 ± 0.62	0.08	6.45
$[Fe^{III}_2(L^3)(solv)_x]^{5+}$	21	5.39	9.38	0.65 ± 0.03	7.38 ± 0.69	0.09	7.44
$[Fe^{III}_2(H_2L^1)(\mu\text{-}O)Cl_2]^{2+}$	22	5.0	7.3	1.33 ± 0.08	1.94 ± 0.37	0.68	6.17
$[Fe^{III}Fe^{II}(BPBPMP)(\mu\text{-}OAc)_2]^+$	32	5.03	6.93	1.88	4.63	0.41	5.6
$[Fe^{III}Fe^{II}(L^3)(solv)_x]^{4+}$	21	5.30	8.02	1.14 ± 0.04	2.30 ± 0.24	0.50	6.69

[a]pH of aqueous buffer solution used for substrate dependence assays. [b]Not available.

signal near $g_{eff} \approx 4.3$ originates from the Fe^{III} center with rhombic symmetry. Such an impurity, but usually with lower intensity, was detected previously in solution EPR spectra of mixed-valent $Fe^{III}Fe^{II}$ complexes.[21,30,32,67] This could arise from a mononuclear rhombic *high-spin* Fe^{III} complex present as impurity, most likely formed by decomposition of $[Fe^{III}Fe^{II}(H_2L^4)(\mu\text{-}OAc)_2]^{2+}$ in solution or a decomposition product of ferrocenium hexafluorophosphate. The latter suggestion is supported by the detection of a similar signal (g_{eff} = 8.56, 5.45, 4.30) from a ferrocenium hexafluorophosphate solution left under aerobic conditions for 2 days. Therefore, it is not clear whether the $Fe^{III}Fe^{II}$ complex generated here is completely stable in solution.

PHOSPHATASE REACTIVITY

The phosphatase reactivity of $[Fe^{II}_2(H_2L^2)(\mu\text{-}OAc)_2]^+$ and $[Fe^{II}_2(H_2L^4)(\mu\text{-}OAc)_2]^+$ was probed with a spectrophotometric assay with BDNPP as a model substrate and a well-established experimental methodology.[23,39,68] The sensitivity of the Fe^{II}_2 complexes to oxidation required measurements to be carried out under inert atmosphere in a glovebox. Because of this experimental complication, the number of data points is smaller and the variance significantly larger than in the experiments with the corresponding Zn^{II}_2 catalysts.[39]

(i). pH Dependence. The plots obtained for the dependence of the initial hydrolysis rate on the pH and on the initial substrate concentration are presented in Figure 11. Because of the relatively small number of data points and the relatively large standard deviations, only a qualitative analysis is appropriate. The initial rate vs pH profiles for $[Fe^{II}_2(H_2L^2)(\mu\text{-}OAc)_2]^+$ and $[Fe^{II}_2(H_2L^4)(\mu\text{-}OAc)_2]^+$ have a similar shape. This is in contrast to the corresponding Zn^{II}_2 complexes of H_3L^2 and H_3L^4,[39] which showed significantly different curve shapes. Under the same conditions, the $[Fe^{II}_2(H_2L^2)(\mu\text{-}OAc)_2]^+$ complex exhibits lower hydrolysis rates than $[Fe^{II}_2(H_2L^4)(\mu\text{-}OAc)_2]^+$. The curve shapes in Figure 11a indicate that three active species are present in the pH range of 7−10: the first deprotonation step at pH ∼7 generates an active species; deprotonation of this species at pH ∼8.5 lowers its activity, while a second deprotonation at pH >9.5 leads to an increase of activity. This behavior is different from that seen for the Zn^{II}_2 compounds $[Zn^{II}_2(H_2L^4)(\mu\text{-}OAc)(OH)]^+$ and $[Zn^{II}_2(H_2L^2)(\mu\text{-}OAc)_2]^+$, which showed a bell-shaped and a sigmoidal profile, respectively.[39]

In contrast to $[Fe^{II}_2(H_2L^4)(\mu\text{-}OAc)_2]^+$, the Fe^{III}_2 complex of ligand H_3L^2 exhibits an initial rate vs pH profile with a relatively sharp activity maximum at pH 6.5.[21] The activity maximum in the region between pH 7 and pH 9 for $[Fe^{II}_2(H_2L^2)(\mu\text{-}OAc)_2]^+$ is at higher pH, compared to $[Fe^{III}_2(H_2L^2)(solv)_x]^{5+}$. This activity shift to higher pH values is in agreement with the pK_a values of iron-bound water molecules (pK_a = 9.5 for Fe^{II} and pK_a = 2.2 for Fe^{III}),[60] following the lower Lewis acidity of Fe^{II}, compared to Fe^{III}.

(ii). Substrate Concentration Dependence. The dependence of the BDNPP hydrolysis rate on the substrate concentration was determined at pH 9.5 to access a catalytically active species of the Fe^{II}_2 complexes and to allow comparison of the studies with the corresponding Zn^{II}_2 complexes.[39] The measurements with the symmetric isomer $[Fe^{II}_2(H_2L^2)(\mu\text{-}OAc)_2]^+$ exhibited hydrolysis rates similar to those of the

DOI: 10.1021/acs.inorgchem.5b00628
Inorg. Chem. XXXX, XXX, XXX−XXX

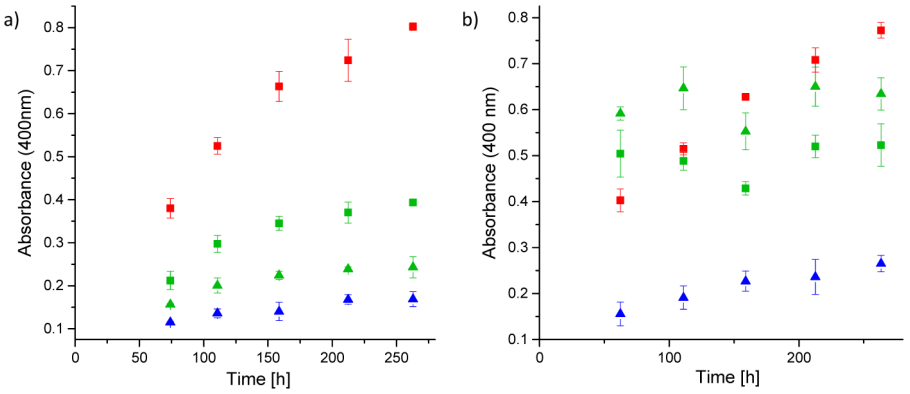

Figure 12. Time dependence of the absorbance band of 2,4-nitrophenolate (400 nm, 25 °C, MeCN−buffer = 1:1, [complex] = 15 nM, [BDNPP] = 5.25 μM, see Experimental Section for details): (a) at pH 9.5 and (b) at pH 11 with $[Zn_2(BPMP)(\mu\text{-}OAc)_2]^+$ (red), $[Fe^{II}_2(H_2L^2)(\mu\text{-}OAc)_2]^+$ (blue), $[Fe^{II}_2(H_2L^4)(\mu\text{-}OAc)_2]^+$ (green squares), and $[Fe^{II}_2(H_2L^4)(\mu\text{-}OAc)_2]^+$ with 1 equiv $Fe^{III}Cp_2PF_6$ (green triangles).

asymmetric isomer $[Fe^{II}_2(H_2L^4)(\mu\text{-}OAc)_2]^+$. Therefore, the activity of these complexes within the first minutes of catalysis appears to be independent of the position of the hydrogen bond donors. The data presented in Figure 11b show Michaelis−Menten saturation behavior. Fitting the data of $[Fe^{II}_2(H_2L^4)(\mu\text{-}OAc)_2]^+$ to the Michaelis−Menten equation (see Experimental Section for details) provides values for the parameters k_{cat}, K_M, and k_{cat}/K_M, which are listed and compared with other diiron PAP model complexes in Table 3.

The impact of the oxidation state of the two Fe centers on the catalysis is shown in a comparison of $[Fe^{III}_2(H_2L^2)(solv)_x]^{5+}$ and $[Fe^{II}_2(H_2L^4)(\mu\text{-}OAc)_2]^+$, which has similar kinetics as $[Fe^{II}_2(H_2L^4)(\mu\text{-}OAc)_2]^+$ (see Figure 11 and the corresponding text). The doubly reduced form exhibits a higher hydrolysis rate, a higher substrate affinity, and, as a consequence, also a higher catalytic efficiency, but requires a more alkaline environment to function optimally. Therefore, the higher activity of the two Fe^{II}_2 complexes studied here, compared to the reference complexes listed in Table 3, can be attributed to the combined effect of hydrogen bonding and the lower Lewis acidity of the two Fe^{II} centers.

Compared to the other examples of phenolate-bridged diiron complexes in Table 3, $[Fe^{II}_2(H_2L^4)(\mu\text{-}OAc)_2]^+$ has the highest hydrolysis rate. In addition, the catalytic efficiency is also one of the highest reported for such systems, and the Michaelis−Menten constant K_M (substrate affinity) is in the medium range of the tabulated diiron complexes.

The substrate concentration dependence measurements conducted with the Zn^{II}_2 complexes $[Zn^{II}_2(H_2L^2)(\mu\text{-}OAc)_2]^+$ and $[Zn^{II}_2(H_2L^4)(\mu\text{-}OAc)(OH)]^+$, also at pH 9.5, resulted for both complexes in lower hydrolysis rates and higher Michaelis−Menten constants than observed for the Fe^{II}_2 complex $[Fe^{II}_2(H_2L^4)(\mu\text{-}OAc)_2]^+$.[39] Consequently, the catalytic efficiencies of $[Zn^{II}_2(H_2L^2)(\mu\text{-}OAc)_2]^+$ and $[Zn^{II}_2(H_2L^4)(\mu\text{-}OAc)(OH)]^+$ are 2- and 4-fold lower, respectively, than that of $[Fe^{II}_2(H_2L^4)(\mu\text{-}OAc)_2]^+$.

(iii). Catalytic Turnover. In order to probe the catalytic behavior of the diiron complexes of ligand H_3L^2 and H_3L^4, studies of their turnover number (TON) were conducted at 25 °C with [complex] = 10 μM and [BDNPP] = 3.0 mM at different pH. The assays were prepared in the glovebox, using 0.5 mM solutions of $[Fe^{II}_2(H_2L^2)(\mu\text{-}OAc)_2]^+$ and $[Fe^{II}_2(H_2L^4)(\mu\text{-}OAc)_2]^+$ as well as a 0.5 mM mixture of $[Fe^{II}_2(H_2L^4)(\mu\text{-}OAc)_2]^+$ with ferrocenium hexafluorophosphate (1:1), prepared 24 h prior to the TON measurements. Samples were taken from these assays at various intervals during the experiments, diluted with solvent, and their UV-vis spectra recorded to determine the amount of phosphoester hydrolysis. The increase in the absorbance at 400 nm, associated with the hydrolysis product 2,4-dinitrophenolate, was monitored over time and TON values were calculated after 9 days. The resulting data obtained at pH 9.5 and pH 11 are given in Figure 12 and Table 4. $[Zn^{II}_2(BPMP)(\mu\text{-}OAc)_2]^+$ was also included in the analysis

Table 4. Turnover Numbers (TONs) of BDNPP Hydrolysis for $[Fe^{II}_2(H_2L^2)(\mu\text{-}OAc)_2]^+$ and $[Fe^{II}_2(H_2L^4)(\mu\text{-}OAc)_2]^+$, as Well as the Mixtures of $[Fe^{II}_2(H_2L^4)(\mu\text{-}OAc)_2]^+$ with 1 equiv of Ferrocenium Hexafluorophosphate

	TON after 9 h		
complex	pH 9	pH 9.5	pH 11
$[Fe^{II}_2(H_2L^2)(\mu\text{-}OAc)_2]^+$	2 ± 2	26 ± 3	37 ± 5
$[Fe^{II}_2(H_2L^4)(\mu\text{-}OAc)_2]^+$	11 ± 2	61 ± 4	86 ± 4
$[Fe^{II}_2(H_2L^4)(\mu\text{-}OAc)_2]^+$ + 1 eq $Fe^{III}Cp_2^+$	6 ± 6	39 ± 1	107 ± 7

to eliminate the possibility of experimental artifacts that are present due to the setup under an inert atmosphere (indeed, the Zn^{II}_2 complex exhibits TONs comparable to those obtained under aerobic conditions).[39] Interestingly, while the Zn^{II}_2 complex does not have any hydrogen bond donors it exhibits the highest TONs of this study.

The TONs for the diiron complexes increase with increasing pH, and all iron complexes have similar TONs at pH <9 (see Supporting Information). However, under more basic conditions, the structural variations in the diiron complexes are reflected in differences of their TONs. Under basic conditions (pH >9), the asymmetric diiron complex $[Fe^{II}_2(H_2L^4)(\mu\text{-}OAc)_2]^+$ (green symbols in Figure 12) shows higher TONs than the symmetric isomer $[Fe^{II}_2(H_2L^2)(\mu\text{-}OAc)_2]^+$ (blue symbols in Figure 12). This is independent of the oxidation state of the Fe centers (i.e., comparison of data in the presence/absence of ferrocenium hexafluorophosphate). It follows that two hydrogen bond donors adjacent to one Fe^{II} center in the Fe^{II}_2 model complex help to prevent product inhibition more efficiently than one hydrogen bond donor adjacent to each Fe^{II} center. Interestingly, the impact of the hydrogen bond donors is therefore the opposite of what was observed with the corresponding Zn^{II}_2 complexes.[39]

As mentioned in the previous section, a comparison of the TONs obtained from assays containing the same Fe^{II}_2 complex

DOI: 10.1021/acs.inorgchem.5b00628
Inorg. Chem. XXXX, XXX, XXX−XXX

with or without the addition of ferrocenium hexafluorophosphate allows the study of the impact of the oxidation states of the Fe centers. The TON of the asymmetric diiron complex (H_3L^4) is dependent on the oxidation state of iron: measurements of TON at pH 9 and pH 9.5 resulted in higher TONs for the reduced form (absence of ferrocenium hexafluorophosphate), indicating that catalysis with the heterovalent catalyst $[Fe^{III}Fe^{II}(H_2L^4)(solv)_x]^{4+}$ is inhibited by a bridging phosphate product. This is in agreement with the higher water exchange rate of Fe^{II}, compared to Fe^{III} (10^6 s^{-1} vs 10^2 s^{-1}).[69−72] However, in a strong base (pH 11), the trend is reversed, i.e., the $Fe^{III}Fe^{II}$ complex of H_3L^4 reveals a higher TON than the Fe^{II}_2 complex. Studies of the hydrolysis of phosphomonoesters using DNPP as model substrate in the TON assays revealed no acceleration of phosphoester hydrolysis compared to the autohydrolysis, independent of the symmetry and the oxidation state of the diiron complexes.

CONCLUSION

The two tetrakis-pyridine ligands H_3L^2 and H_3L^4, symmetrical and asymmetrical, respectively, in terms of hydrogen bonding, produce, under anaerobic conditions, $[Fe^{II}_2(H_2L^2)(\mu\text{-}OAc)_2]$-$PF_6$ and $[Fe^{II}_2(H_2L^4)(\mu\text{-}OAc)_2]PF_6$ with structures as expected for phenoxido-bridged phosphatase models. Under aerobic conditions only the monoiron Fe^{III}/Na^+ complex $[Fe^{III}Na(H_2L^4)(\mu\text{-}OAc)_2]PF_6$ could be isolated and structurally characterized.

In the solid and in solution, $[Fe^{II}_2(H_2L^4)(\mu\text{-}OAc)_2]PF_6$ consists of two weakly antiferromagnetically coupled *high-spin* Fe^{II} centers with identical first but different second coordination spheres. Cyclic voltammetry indicates that $[Fe^{II}_2(H_2L^4)(\mu\text{-}OAc)_2]^+$ has two reasonably well-separated redox waves (Fe^{II}_2/$Fe^{III}Fe^{II}$ and $Fe^{III}Fe^{II}$/Fe^{III}_2) with a comproportionation constant K_{com} of 8.5×10^6. Therefore, the heterovalent diiron complex $[Fe^{III}Fe^{II}(H_2L^4)(solv)_x]^{4+}$, obtained by oxidation of $[Fe^{II}_2(H_2L^4)(\mu\text{-}OAc)_2]^+$ with ferrocenium hexafluorophosphate under anaerobic conditions, could be trapped and characterized by ^{57}Fe Mössbauer, UV-vis, and EPR spectroscopy. $[Fe^{III}Fe^{II}(H_2L^4)(solv)_x]^{4+}$ is an accurate structural model for the active form of mammalian PAPs with a heterovalent diiron core in an asymmetric geometry and, since it is phosphatase catalyst, it also is a functional model. However, the relatively low comproportionation constant indicates that the heterovalent complex is not very stable.

The phosphoester hydrolysis studies of the Fe^{II}_2 complexes of the tetrakis-pyridine ligands H_3L^2 and H_3L^4, and the $Fe^{III}Fe^{II}$ form of H_3L^4, in comparison with the corresponding Zn^{II}_2 complexes, reveal that the activity depends on the secondary coordination sphere and the Lewis acidity of the metal ion. The initial hydrolysis rate seems to be independent of the geometry of hydrogen bonding but the TONs are influenced by the symmetry of the hydrogen bonding network. Interestingly, the effect of the position of the pivaloylamide residues for the corresponding Zn^{II}_2 complexes is quite different, and this indicates that the steric bulk of the pivaloylamide groups and semicoordination of the amide oxygen groups also are important and obviously different for Fe^{II}, Fe^{III}, and Zn^{II} centers. Because of the higher Lewis acidity and slower water exchange rates, the Fe^{II}_2 complexes have lower TONs and higher hydrolysis rates and catalytic efficiencies than the Zn^{II}_2 complexes. Therefore, as expected for a decrease of the water exchange rate and the higher Lewis acidity of Fe^{III}, relative to Fe^{II},[41,73] the oxidation of one of the two Fe^{II} centers in $[Fe^{II}_2(H_2L^4)(\mu\text{-}OAc)_2]^+$ to a mixed valence $Fe^{III}Fe^{II}$ complex leads to a decrease of the TON. With H_2L^2, the Fe^{II}_2 complex reveals a more basic pH maximum than the corresponding Fe^{III}_2 complex, i.e., the role of the Fe^{III} center in the active site of PAP is the provision of a nucleophilic hydroxide at low pH, and the mixed valent diiron complex of H_3L^4 with an asymmetric disposition of the hydrogen bond donors therefore is an accurate structural and functional model of PAPs.

EXPERIMENTAL SECTION

(i). NMR Spectroscopy. Nuclear magnetic resonance (NMR) spectra were recorded with a Bruker Model AV500 spectrometer. Chemical shifts are reported in units of δ, relative to the known solvent peak reference: δ_H = 1.94 ppm for CD_3CN; the symbol "s" was used as abbreviation for a singlet. The software package TopSpin from BRUKER was used for data processing.[74]

(ii). Magnetic Susceptibility Measurement by the Evans Method. Magnetic moments in solution were measured for a solution of known concentration of complex in CD_3CN in a capillary which was in a NMR tube carrying the same solvent. The experiments were conducted with a Bruker AV500 instrument. Magnetic moments were evaluated using eqs 5 and 6,

$$\chi_{para,subst} = \frac{3}{4\pi c}\left(\frac{\Delta\nu}{\nu}\right) + \chi_{dia,solv} + \chi_{dia,subst} \quad (5)$$

$$\mu = 2.828\sqrt{\chi_{para,subst}\,T} \quad (6)$$

and appropriate corrections were considered.[51]

(iii). Solid-State Magnetic Susceptibility Measurement with SQUID Magnetometry. Magnetic susceptibility in solid state were examined with a MPMS-XL 5T superconducting quantum interference device (SQUID) from Quantum Design. The powdered samples were pressed into a PTFE band to avoid field-induced orientation and incorporated into two plastic straws as sample holder. Diamagnetic corrections for the PTFE band and the sample holder were applied.

(iv). X-ray Structure Analyses. X-ray crystallographic data were collected with a Bruker AXS Smart 1000 CCD and an Agilent Technologies SuperNova-E dual source (Mo or Cu) CCD diffractometer.[75−79] Using the software Olex2,[80] the structures were solved by iterative methods (SUPERFLIP)[81,82] and refined by full matrix least-squares methods based on F^2 (SHELXL Version 2014/6).[83,84] In case of $[Fe^{II}_2(H_2L^2)(\mu\text{-}OAc)_2]PF_6$ the structure was refined with a diethyl ether solvate in the crystal cell. For $[Fe^{II}_2(H_2L^1)(\mu\text{-}OAc)_2]PF_6$ and $\{Na[Fe^{II}_2(H_2L^5)(\mu\text{-}OAc)_2]_2\}PF_6$ (see Supporting Information) electron density attributed to disordered solvent was removed from the structure with the BYPASS procedure as implemented in PLATON (SQUEEZE).[85−87] Partial structure factors from the solvent masks were included in the refinement as separate contributions to F_{obs}. All non-hydrogen atoms were given anisotropic displacement parameters, unless they were disordered and were placed at calculated positions. Hydrogen atoms were fixed geometrically and were not refined. The X-ray structural data of the published structures were deposited with the Cambridge Crystallographic Data Centre (CCDC).

(v). Mass Spectrometry. High-resolution mass spectra were collected with a Bruker microTOFQ ESI-MS spectrometer in the School of Chemistry and Molecular Biosciences at the University of Queensland and a Bruker Apex-Qe hybrid 9.4 T FT-ICR instrument at the Institute of Organic Chemistry at the University of Heidelberg. The data were processed with Bruker Compass Data Analysis software.

(vi). Elemental Analyses. Elemental microanalyses were performed in the analytic laboratories of the Institute of Organic Chemistry at the University of Heidelberg with an Elementar Vario Mikro cube machine and the Carlo Erba Elemental Analyzer (Model NA1500) in the School of Chemistry and Molecular Biosciences at the University of Queensland.

(vii). Cyclic Voltammetry. Cyclic voltammetric measurements were performed on a CH Instruments Model CHI660D electro-

DOI: 10.1021/acs.inorgchem.5b00628
Inorg. Chem. XXXX, XXX, XXX−XXX

chemical workstation equipped with a Faraday cage using a three-electrode setup consisting of a glassy carbon working electrode, a platinum wire as a counter electrode, and a Ag/Ag^+ (0.1 mM in NaCl) reference electrode. The complex solutions were prepared with degassed solvents with 0.1 M NBu_4ClO_4 as the electrolyte. The redox potentials of the signals obtained were determined by comparison to a ferrocene sample measured under the same conditions and referenced vs SCE ($E(Fc/Fc^+)$ = 0.380 V vs SCE).[46]

(viii). EPR Spectroscopy. X-band EPR spectra were measured with a Bruker Model Biospin ELEXSYS E500 spectrometer. The microwave frequency and magnetic field were calibrated with a Bruker frequency counter and an ER036 TM or an ER035 M Tesla meter. Spin-Hamiltonian parameters were determined by computer simulations of the experimental spectra using the programs XSophe and MoSophe.[88,89] The simulated and experimental spectra were visualized with the software suite XeprView.[90,91]

(ix). UV-vis-NIR Spectroscopy. UV-vis-NIR spectra were recorded at 25 °C with a TIDAS II J&M spectrophotometer and a Varian Cary50 Bio UV/visible spectrophotometer in 10 mm quartz cuvettes. Time-dependent UV-vis-NIR measurements were performed using a TIDAS II J&M spectrophotometer. Time-course measurements at fixed wavelengths were monitored by a JASCO Model V-570 spectrophotometer and a Varian Cary50 Bio UV/visible spectrophotometer with a Peltier temperature controller.

(x). Mössbauer Spectroscopy. ^{57}Fe Mössbauer spectra of frozen solutions were acquired with a conventional spectrometer incorporating an Oxford Instruments Mössbauer-Spectromag 4000 Cryostat, equipped with a ^{57}Co source (3.7 GBq) in a rhodium matrix in the constant-acceleration mode at 170 K. Isomer shifts are given relative to α-Fe at 300 K. Spectra were fitted using the NORMOS Mössbauer Fitting Program.[61]

(xi). Synthesis of Complexes. The ligands H_3L^2, H_3L^4 and H_4L^5 were prepared as described previously.[21,39]

(xii). Synthesis of Dinuclear Fe^{II} Complexes. The ligand (68.6 μmol) was dissolved under inert atmosphere in anhydrous, degassed methanol (2.5 mL). The solution was treated with iron^{II} acetate (137 μmol) and stirred at room temperature overnight. Sodium hexafluorophosphate (140 μmol) was added and the mixture stirred for 10 min before filtration through a syringe filter. Crystallization from the filtrate was achieved with diffusion of diethyl ether, whereby yellow crystals were obtained, which were collected by filtration.

$[Fe^{II}_2(H_2L^2)(\mu\text{-}OAc)_2]PF_6$ (48.2 mg, 63%): ^{1}H NMR (500.13 MHz, CD_3CN): δ = 2.12 (s, 2H), 5.40 (s, 18H), 5.68 (s, 2H), 5.76 (s, 2H), 10.70 (bs, 2H), 13.00 (bs, 2H), 17.06 (s, 2H), 26.15 (s, 2H), 29.54 (s, 3H), 41.15 (s, 3H), 41.37 (s, 5H), 45.70 (bs, 2H), 55.14 (s, 2H), 57.07 (s, 2H), 80.81 (bs, 2H), 107.33 (bs, 2H), 157.62 (bs, 2H), 188.50 (s, 2H) ppm. HRMS (ESI^+, CH_2Cl_2): m/z = 957.3074 ($[C_{47}H_{57}N_8O_7Fe_2]^+$, *calcd.* 957.3046). Elemental analysis (%) *calcd.* for $C_{47}H_{57}N_8O_7Fe_2PF_6$: C, 51.20; H, 5.21; N, 10.16; found: C, 51.28; H, 5.46; N, 10.20.

$[Fe^{II}_2(H_2L^4)(\mu\text{-}OAc)_2]PF_6$ (37.0 mg; 49%): ^{1}H NMR (500.13 MHz, CD_3CN): δ = −31.71 (bs, 1H), −17.11 (bs, 1H), −12.52 (bs, 1H), −5.86 (bs, 1H), −1.20 (s, 1H), 3.86 (s, 9H), 4.08 (s, 9H), 7.49 (s, 1H), 9.48 (s, 1H), 9.67 (s, 1H), 12.52 (s, 1H), 17.21 (bs, 1H), 22.61 (s, 1H), 27.49 (s, 1H), 32.89 (s, 1H), 36.04 (s, 1H), 36.11 (s, 4H), 41.10 (s, 3H), 41.55 (s, 1H), 46.06 (s, 1H), 50.39 (s, 2H), 52.42 (s, 1H), 57.01 (s, 3H), 67.36 (s, 1H), 69.39 (s, 1H), 73.79 (s, 1H), 77.16 (s, 1H), 93.51 (s, 1H), 120.21 (bs, 1H), 148.20 (bs, 1H), 166.91 (s, 1H), 189.14 (s, 1H) ppm. HRMS (ESI^+, CH_2Cl_2): m/z = 957.3087 ($[C_{47}H_{57}N_8O_7Fe_2]^+$, *calcd.* 957.3046). Elemental analysis (%) *calcd.* for $C_{47}H_{57}N_8O_7Fe_2PF_6$: C, 51.20; H, 5.21; N, 10.16; *found*: C, 51.17; H, 5.30; N, 10.05.

(xiii). Synthesis of $[Fe^{III}Na(H_2L^4)(\mu\text{-}OAc)_2]PF_6$. H_3L^4 (68.6 μmol) was dissolved under inert atmosphere in anhydrous, degassed methanol (2.5 mL). The solution was treated with iron(II) acetate (137 μmol) and stirred at room temperature overnight. Sodium hexafluorophosphate (140 μmol) was added and the mixture stirred for 10 min before filtration through a syringe filter. The yellow solution was treated with degassed diethyl ether (2.0 mL) and exposed to air. Crystallization was achieved with diffusion of diethyl ether, whereby purple crystals were obtained, which were collected by filtration. The unusual presence of a Na^+ ion with a phenolate-based ligand was additionally confirmed by elemental analysis. The calculation of the molecular formula derived from the analytical data is $C_{48}H_{49}N_8F_6FeNa$, which compares to the required molecular formula $C_{47}H_{57}N_8O_7F_6FeNa$ for $[Fe^{III}Na(H_2L^4)(\mu\text{-}OAc)_2]PF_6$ and proves the Fe:Na ratio of 1:1. Elemental analysis (%) *calcd.* for $C_{47}H_{57}N_8O_7FeNaPF_6$: C, 52.77; H, 5.37; N, 10.47; F, 10.66; Fe, 5.22; Na, 2.15; *found*: C. 51.11; H, 4.62; N, 9.96; F, 10.17; Fe, 5.84; Na, 2.27.

(xiv). Kinetic Assays. Phosphoester hydrolysis activity of the complexes was probed with a spectrophotometric assay using BDNPP as phosphodiester model substrate. BDNPP was synthesized following published procedures with minor modifications.[92] Cleavage of the phosphorus−oxygen bond was followed at 25 °C by monitoring the generated product, 2,4-dinitrophenolate, by its strong absorption at 400 nm (ε = 12 100 M^{-1} cm^{-1}). All measurements were carried out in 1:1 acetonitrile−buffer mixtures and performed in triplicate. The complex was allowed to equilibrate in the acetonitrile−buffer mixture for 1 min prior to the addition of substrate. When the substrate was added to the reaction mixture, the starting hydrolysis activity was monitored in the time between 15 s and 195 s and analyzed by linear regression. For each experiment, autohydrolysis assays were conducted by measuring the hydrolysis rate under the same conditions, but lacking the catalyst, and were subtracted from the derived data. The aqueous buffer consisted of 2-(*N*-morpholino)ethanesulfonic acid (MES) (50 mM; pH range: 5.5−6.7), 4-(2-hydroxyethyl)piperazine-1-ethanesulfonic acid (HEPES) (50 mM; pH range: 6.8−8.2), 2-(cyclohexylamino)ethanesulfonic acid (CHES) (50 mM; pH range: 8.6−10.0), 3-(cyclohexylamino)-1-propanesulfonic acid (CAPS) (50 mM; pH range: 9.7−11.1) and lithium perchlorate (250 mM) for ionic strength control. The desired pH of the buffers was adjusted by addition of aqueous sodium hydroxide solution. Following treatment with Chelex, (Chelex 100, sodium form) overnight and filtration with 45 μm syringe filters ensured the absence of additional metal ions in the buffer solutions. The pH values reported refer to the aqueous component; however, note that the pH of a 1:1 mixture of buffer and acetonitrile was the same, within error, as that of the corresponding buffer solution itself.[93,94] The activated model substrate BDNPP was initially prepared as 15 mM solution in acetonitrile and the complex solutions were 1 mM in acetonitrile. The pH dependence of the activity was studied by varying the pH value of the multicomponent buffer in the pH range of 5−11. In this process, the assays contained the complex 0.04 mM and BDNPP 5 mM in the cuvette. Substrate concentration dependence of the catalytic rate was examined with a fixed complex concentration of 0.04 mM and various BDNPP concentrations. Studies of the turnover number (TON) were conducted using a complex concentration of 15 nM and a BDNPP concentration of 5.25 μM. Samples were taken at various intervals during the experiment, diluted with solvent, and their UV-vis spectra were recorded to determine the progress of phosphoester hydrolysis. The increase in the absorbance at 400 nm, assigned to the hydrolysis product 2,4-dinitrophenolate, was monitored over time and TON values were calculated using the Beer−Lambert Law.

■ ASSOCIATED CONTENT

Ⓢ Supporting Information

The Supporting Information includes details of the crystallographic experiments, ORTEP plots of all molecular structures with 50% probability level of thermal ellipsoids, and the spectroscopic characterization of the compounds used, as well as details on the kinetic studies. CCDC Nos. 1054873−1054876 contain supplementary crystallographic data. The Supporting Information is available free of charge on the ACS Publications website at DOI: 10.1021/acs.inorgchem.5b00628.

DOI: 10.1021/acs.inorgchem.5b00628
Inorg. Chem. XXXX, XXX, XXX−XXX

AUTHOR INFORMATION

Corresponding Author

*Fax: +49-6221-546617. E-mail: peter.comba@aci.uni-heidelberg.de.

Notes

The authors declare no competing financial interest.

◆Deceased.

ACKNOWLEDGMENTS

Financial support by the German Science Foundation (DFG), the German Academic Exchange Program (DAAD), and the University of Heidelberg are gratefully acknowledged. G.S. acknowledges a Future Fellowship from the Australian Research Council (No. FT120100694).

REFERENCES

(1) Abu-Omar, M. M.; Loaiza, A.; Hontzeas, N. *Chem. Rev.* **2005**, *105*, 2227−2252.

(2) McDonald, A. R.; Que, L., Jr. *Coord. Chem. Rev.* **2013**, *257*, 414−428.

(3) Comba, P. In *Molecular Catalysis*; Gade, L. H.,Hofmann, P., Eds.; Wiley−VCH: Weinheim, Germany, 2014; pp 123−145.

(4) Mitić, N.; Smith, S. J.; Neves, A.; Guddat, L. W.; Gahan, L. R.; Schenk, G. *Chem. Rev.* **2006**, *106*, 3338−3363.

(5) Schenk, G.; Mitić, N.; Hanson, G.; Comba, P. *Coord. Chem. Rev.* **2013**, *257*, 473−482.

(6) Antanaitis, B. C.; Aisen, P.; Lilienthal, H. R. *J. Biol. Chem.* **1983**, *258*, 3166−3172.

(7) Wilkins, R. G. *Chem. Soc. Rev.* **1992**, *21*, 171−178.

(8) Averill, B. A.; Davis, J. C.; Burman, S.; Zirino, T.; Sanders-Loehr, J.; Loehr, T. M.; Sage, J. T.; Debrunner, P. G. *J. Am. Chem. Soc.* **1987**, *109*, 3760−3767.

(9) Yang, Y.-S.; McCormick, J. M.; Solomon, E. I. *J. Am. Chem. Soc.* **1997**, *119*, 11832−11842.

(10) Lee, J.; Jung, D. J.; Lee, H.-J.; Lee, K.-B.; Hur, N. H.; Jang, H. G. *Bull. Korean Chem. Soc.* **2000**, *21*, 1025−1030.

(11) Merkx, M.; Averill, B. A. *Biochemistry* **1998**, *37*, 11223−11231.

(12) Klabunde, T.; Krebse, B. In *Metal Sites in Proteins and Models*; Hill, H. A. O., Sadler, P. J., Thompson, A. J., Eds.; Structure and Bonding, Vol. *89* Springer: Berlin, Heidelberg, 1997, pp 177−198.

(13) Wang, D. L.; Holz, R. C.; David, S. S.; Que, L., Jr.; Stankovich, M. T. *Biochemistry* **1991**, *30*, 8187−8194.

(14) Bernhardt, P. V.; Schenk, G.; Wilson, G. J. *Biochemistry* **2004**, *43*, 10387−10392.

(15) Debrunner, P. G.; Hendrich, M. P.; J. de Jersey, Keough, D. T.; Sage, J. T.; Zerner, B. *Biochim. Biophys. Acta, Protein Struct. Mol. Enzymol.* **1983**, *745*, 103−106.10.1016/0167-4838(83)90175-9

(16) Rodriguez, J. H.; Ok, H. N.; Xia, Y. M.; Debrunner, P. G.; Hinrichs, B. E.; Meyer, T.; Packard, N. H. *J. Phys. Chem.* **1996**, *100*, 6849−6862.

(17) Day, E. P.; David, S. S.; Peterson, J.; Dunham, W. R.; Bonvoisin, J. J.; Sands, R. H.; Que, L., Jr. *J. Biol. Chem.* **1988**, *263*, 15561−15567.

(18) Dietrich, M.; Münstermann, D.; Suerbaum, H.; Witzel, H. *Eur. J. Biochem.* **1991**, *199*, 105−113.

(19) Oddie, G. W.; Schenk, G.; Angel, N. Z.; Walsh, N.; Guddat, L. W.; de Jersey, J.; Cassady, A. I.; Hamilton, S. E.; Hume, D. A. *Bone* **2000**, *27*, 575−584.

(20) Valizadeh, M.; Schenk, G.; Nash, K.; Oddie, G. W.; Guddat, L. W.; Hume, D. A.; de Jersey, J.; Burke, T. R.; Hamilton, S. *Arch. Biochem. Biophys.* **2004**, *424*, 154−162.

(21) Comba, P.; Gahan, L. R.; Mereacre, V.; Hanson, G. R.; Powell, A. K.; Schenk, G.; Zajaczkowski-Fischer, M. *Inorg. Chem.* **2012**, *51*, 12195−12209.

(22) Comba, P.; Gahan, L. R.; Hanson, G. R.; Mereacre, V.; Noble, C. J.; Powell, A. K.; Prisecaru, I.; Schenk, G.; Zajaczkowski-Fischer, M. *Chem.—Eur. J.* **2012**, *18*, 1700−1710.

(23) Gahan, L. R.; Smith, S. J.; Neves, A.; Schenk, G. *Eur. J. Inorg. Chem.* **2009**, *2009*, 2745−2758.

(24) Neves, A.; de Brito, M. A.; Vencato, I.; Drago, V.; Griesar, K.; Haase, W.; Mascarenhas, Y. P. *Inorg. Chim. Acta* **1993**, *214*, 5−8.

(25) Krebs, B.; Schepers, K.; Bremer, B.; Henkel, G.; Althaus, E.; Müller-Warmuth, W.; Griesar, K.; Haase, W. *Inorg. Chem.* **1994**, *33*, 1907−1914.

(26) Eulering, B.; Ahlers, F.; Zippel, F.; Schmidt, M.; Nolting, H. F.; Krebs, B. *J. Chem. Soc., Chem. Commun.* **1995**, 1305−1307.

(27) Nie, H. L.; Aubin, S. M. J.; Mashuta, M. S.; Wu, C. C.; Richardson, J. F.; Hendrickson, D. N.; Buchanan, R. M. *Inorg. Chem.* **1995**, *34*, 2382.

(28) Borovik, A. S.; Papaefthymiou, V.; Taylor, L. F.; Anderson, O. P.; Que, L. *J. Am. Chem. Soc.* **1989**, *111*, 6183−6195.

(29) Suzuki, M.; Uehara, A.; Oshio, H.; Endo, K.; Yanaga, M.; Kida, S.; Saito, K. *Bull. Chem. Soc. Jpn.* **1987**, *60*, 3547−3555.

(30) Yim, S. H.; Lee, H. J.; Lee, K.-B.; Kang, S. J.; Hur, N. H.; Jang, H. G. *Bull. Korean Chem. Soc.* **1998**, *19*, 654−660.

(31) Albedyhl, S.; Averbuch-Pouchot, M. T.; Belle, C.; Krebs, B.; Pierre, J. L.; Saint-Aman, E.; Torelli, S. *Eur. J. Inorg. Chem.* **2001**, *2001*, 1457−1464.

(32) Smith, S. J.; Peralta, R. A.; Jovito, R.; Horn, J. A.; Bortoluzzi, A. J.; Noble, C. J.; Hanson, G. R.; Stranger, R.; Jayaratne, V.; Cavigliasso, G.; Gahan, L. R.; Schenk, G.; Nascimento, O. R.; Cavalett, A.; Bortolotto, T.; Razzera, G.; Terenzi, H.; Neves, A.; Riley, M. *Inorg. Chem.* **2012**, *51*, 2065−2078.

(33) Neves, A.; Aires de Brito, M. A.; Drago, V.; Griesar, K.; Haase, W. *Inorg. Chim. Acta* **1995**, *237*, 131−135.

(34) Karsten, P.; Neves, A.; Bortoluzzi, A. J.; Lanznaster, M.; Drago, V. *Inorg. Chem.* **2002**, *41*, 4624−4626.

(35) Lambert, E.; Chabut, B.; Chardon-Noblat, S.; Deronzier, A.; Chottard, G.; Bousseksou, A.; Tuchagues, J.-P.; Laugier, J.; Bardet, M.; Latour, J.-M. *J. Am. Chem. Soc.* **1997**, *119*, 9424−9437.

(36) Batista, S. C.; Neves, A.; Bortoluzzi, A. J.; Vencato, I.; Peralta, R. A.; Szpoganicz, B.; Aires, V. V. E.; Terenzi, H.; Severino, P. C. *Inorg. Chem. Commun.* **2003**, *6*, 1161−1165.

(37) Funhoff, E. G.; Wang, W. L.; Andersson, G.; Averill, B. A. *FEBS J.* **2005**, *272*, 2968−2977.

(38) Zajaczkowski-Fischer, M. S. Ph.D. Thesis, Heidelberg University, Heidelberg, Germany, 2010.

(39) Bosch, S.; Comba, P.; Gahan, L. R.; Schenk, G. *Inorg. Chem.* **2014**, *53*, 9036−9051.

(40) Inomata, T.; Shinozaki, K.; Hayashi, Y.; Arii, H.; Funahashi, Y.; Ozawa, T.; Masuda, H. *Chem. Commun.* **2008**, 392−394.

(41) Richens, D. T. *The chemistry of aqua ions: Synthesis, structure and reactivity: A tour through the periodic table of the elements*; Wiley: Chichester, U.K., 1997.

(42) O'Connor, C. J.; Lippard, S. J. *Magnetochemistry—Advances in Theory and Experimentation*; Progress in Inorganic Chemistry, Vol. 29; Wiley: Hoboken, NJ, 1982203−283 (DOI: 10.1002/9780470166307.ch4).

(43) Jang, H. G.; Hendrich, M. P.; Que, L., Jr. *Inorg. Chem.* **1993**, *32*, 911−918.

(44) Tolman, W. B.; Liu, S.; Bentsen, J. G.; Lippard, S. J. *J. Am. Chem. Soc.* **1991**, *113*, 152−164.

(45) Grillo, V. A.; Hanson, G. R.; Hambley, T. W.; Gahan, L. R.; Murray, K. S.; Moubaraki, B. *J. Chem. Soc., Dalton Trans.* **1997**, 305−311.

(46) Pavlishchuk, V. V.; Addison, A. W. *Inorg. Chim. Acta* **2000**, *298*, 97−102.

(47) Alimi, M.; Allam, A.; Selkti, M.; Tomas, A.; Roussel, P.; Galardon, E.; Artaud, I. *Inorg. Chem.* **2012**, *51*, 9350−9356.

(48) Rivas, J. C. M.; Hinchley, S. L.; Metteau, L.; Parsons, S. *Dalton Trans.* **2006**, 2316−2322.

(49) Manago, T.; Hayami, S.; Oshio, H.; Osaki, S.; Hasuyama, H.; Herber, R.; Maeda, Y. *J. Chem. Soc., Dalton Trans.* **1999**, 1001−1012.

(50) Bertini, I.; Luchinat, C.; Parigi, G. *Solution NMR of Paramagnetic Molecules: Applications to Metallobiomolecules and Models*; Elsevier: Amsterdam, 2001.

DOI: 10.1021/acs.inorgchem.5b00628
Inorg. Chem. XXXX, XXX, XXX−XXX

(51) Evans, D. F. *J. Chem. Soc.* **1959**, 2003−2005.
(52) Gebala, A. E.; Jones, M. M. *J. Inorg. Nucl. Chem.* **1969**, *31*, 771−776.
(53) Wiedemann, D.; Swietek, E.; Macyk, W.; Grohmann, A. *Z. Anorg. Allg. Chem.* **2013**, *639*, 1483−1490.
(54) Buchholz, R. R.; Etienne, M. E.; Dorgelo, A.; Mirams, R. E.; Smith, S. J.; Chow, S. Y.; Hanton, L. R.; Jameson, G. B.; Schenk, G.; Gahan, L. R. *J. Chem. Soc., Dalton Trans.* **2008**, 6045−6054.
(55) Daumann, L. J.; Dalle, K. E.; Schenk, G.; McGeary, R. P.; Bernhardt, P. V.; Ollis, D. L.; Gahan, L. R. *Dalton Trans.* **2012**, *41*, 1695−1708.
(56) Zheng, S.; Berto, T. C.; Dahl, E. W.; Hoffman, M. B.; Speelman, A. L.; Lehnert, N. *J. Am. Chem. Soc.* **2013**, *135*, 4902−4905.
(57) Yan, S.; Cheng, P.; Wang, Q.; Liao, D.; Jiang, Z.; Wang, G. *Sci. China, Ser. B: Chem.* **2000**, *43*, 405−411.
(58) Ainscough, E. W.; Brodie, A. M.; Plowman, J. E.; Brown, K. L.; Addison, A. W.; Gainsford, A. R. *Inorg. Chem.* **1980**, *19*, 3655−3663.
(59) Gaber, B. P.; Miskowski, V.; Spiro, T. G. *J. Am. Chem. Soc.* **1974**, *96*, 6868−6873.
(60) Baes, C. F.; Mesmer, R. E. *The hydrolysis of cations*; Wiley:New York, 1976.
(61) *NORMOS-90 Mossbauer Fitting Program Package*; R. A. Brandt: Duisburg, Germany, 1994.
(62) Hayashi, Y.; Kayatani, T.; Sugimoto, H.; Suzuki, M.; Inomata, K.; Uehara, A.; Mizutani, Y.; Kitagawa, T.; Maeda, Y. *J. Am. Chem. Soc.* **1995**, *117*, 11220−11229.
(63) Chen, J.; Wang, X.; Zhu, Y.; Lin, J.; Yang, X.; Li, Y.; Lu, Y.; Guo, Z. *Inorg. Chem.* **2005**, *44*, 3422−3430.
(64) Xavier, F. R.; Peralta, R. A.; Bortoluzzi, A. J.; Drago, V.; Castellano, E. E.; Haase, W.; Tomkowicz, Z.; Neves, A. *J. Inorg. Biochem.* **2011**, *105*, 1740−1752.
(65) Borovik, A. S.; Que, L. *J. Am. Chem. Soc.* **1988**, *110*, 2345.
(66) Maeda, Y.; Yamamoto, M.; Hayami, S. *J. Radioanal. Nucl. Chem.*, **2007**, *272*, 651−656.10.1007/s10967-007-0640-0
(67) Suzuki, M.; Oshio, H.; Uehara, A.; Endo, K.; Yanaga, M.; Kida, S.; Saito, K. *Bull. Chem. Soc. Jpn.* **1988**, *61*, 3907−3913.
(68) Desbouis, D.; Troitsky, I. P.; Belousoff, M. J.; Spiccia, L.; Graham, B. *Coord. Chem. Rev.* **2012**, *256*, 897−937.
(69) Kantacha, A.; Buchholz, R.; Smith, S.; Schenk, G.; Gahan, L. *JBIC, J. Biol. Inorg. Chem.* **2011**, *16*, 25−32.
(70) Helm, L.; Merbach, A. E. *Chem. Rev. (Washington, DC, U. S.)* **2005**, *105*, 1923−1959.
(71) Tanaka, M.; Yamada, S. *J. Chem. Soc., Chem. Commun.* **1976**, 178−179.
(72) Grant, M.; Jordan, R. B. *Inorg. Chem.* **1981**, *20*, 55−60.
(73) Lide, D. R. *CRC Handbook of Chemistry and Physics: A Ready-Reference Book of Chemical and Physical Data*, 89th Edition; CRC Press: Boca Raton, FL, 2008.
(74) *TopSpin 2.0, Software for NMR data processing*; Bruker: Karlsruhe, Germany.
(75) *SAINT*; Bruker AXS: Karlsruhe, Germany, 1997−2013.
(76) *CrysAlisPro*; Agilent Technologies UK, Ltd., Oxford, U.K., 2011−2013.
(77) Blessing, R. H. *Acta Crystallogr., Sect. A: Found. Crystallogr.* **1995**, *A51*, 33−38.
(78) Sheldrick, G. M. Bruker AXS: Karlsruhe, Germany, 2004−2014.
(79) *CrysAlisPro SCALE3 ABSPACK*, Agilent Technologies UK, Ltd., Oxford, U.K., 2011−2014.
(80) Dolomanov, O. V.; Bourhis, L. J.; Gildea, R. J.; Howard, J. A. K.; Puschmann, H. *J. Appl. Crystallogr.* **2009**, *42*, 339−341.
(81) Palatinus, L. *SUPERFLIP*; EPFL: Lausanne, Switzerland, 2007.
(82) Palatinus, L.; Chapuis, G. *J. Appl. Crystallogr.* **2007**, *40*, 786−790.
(83) Sheldrick, G. M. *Acta Crystallogr., Sect. A: Found. Crystallogr.* **2008**, *A64*, 112−122.
(84) Sheldrick, G. M. *SHELXL-2013*, University of Göttingen: Göttingen, Germany, 2013.
(85) van der Sluis, P.; Spek, A. L. *Acta Crystallogr., Sect. A: Found. Crystallogr.* **1990**, *A46*, 194−201.
(86) Spek, A. L. *J. Appl. Crystallogr.* **2003**, *36*, 7−13.
(87) Spek, A. L. *Acta Crystallogr.* **2015**, *C71*, 9−18.
(88) Hanson, G. R.; Gates, K. E.; Noble, C. J.; Griffin, M.; Mitchell, A.; Benson, S. *J. Inorg. Biochem.* **2004**, *98*, 903−916.
(89) Hanson, G. *Biospin*; Bruker : Germany, 2007.
(90) Wang, D.; Hanson, G. R. *J. Magn. Reson., Ser. A* **1995**, *117*, 1−8.
(91) Wang, D.; Hanson, G. R. *Appl. Magn. Reson.* **1996**, *11*, 401−415.
(92) Bunton, C. A.; Farber, S. J. *J. Org. Chem.* **1969**, *34*, 767−772.
(93) Daumann, L. J.; Gahan, L. R.; Comba, P.; Schenk, G. *Inorg. Chem.* **2012**, *51*, 7669−7681.
(94) Daumann, L.; Marty, L.; Schenk, G.; Gahan, L. R. *Dalton Trans.* **2013**, *42*, 9574−9584.

DOI: 10.1021/acs.inorgchem.5b00628
Inorg. Chem. XXXX, XXX, XXX−XXX